remote sensing

MDPI

Article

Multi-View Polarimetric Scattering Cloud Tomography and Retrieval of Droplet Size

Aviad Levis [1,*,†], Yoav Y. Schechner [1], Anthony B. Davis [2] and Jesse Loveridge [3]

[1] Viterbi Faculty of Electrical Engineering, Technion - Israel Institute of Technology, Haifa 3200003, Israel; yoav@ee.technion.ac.il
[2] Jet Propulsion Laboratory, California Institute of Technology, Pasadena, CA 91109, USA; Anthony.B.Davis@jpl.nasa.gov
[3] Department of Atmospheric Sciences, University of Illinois, Champaign, IL 61820, USA; jesserl2@illinois.edu
* Correspondence: aviad.levis@gmail.com
† Current Address: Computing and Mathematical Sciences Department, California Institute of Technology, Pasadena, CA 91125, USA.

Received: 30 July 2020; Accepted: 28 August 2020; Published: 1 September 2020

Abstract: Tomography aims to recover a three-dimensional (3D) density map of a medium or an object. In medical imaging, it is extensively used for diagnostics via X-ray computed tomography (CT). We define and derive a tomography of cloud droplet distributions via passive remote sensing. We use multi-view polarimetric images to fit a 3D polarized radiative transfer (RT) forward model. Our motivation is 3D volumetric probing of vertically-developed convectively-driven clouds that are ill-served by current methods in operational passive remote sensing. Current techniques are based on strictly 1D RT modeling and applied to a single cloudy pixel, where cloud geometry defaults to that of a plane-parallel slab. Incident unpolarized sunlight, once scattered by cloud-droplets, changes its polarization state according to droplet size. Therefore, polarimetric measurements in the rainbow and glory angular regions can be used to infer the droplet size distribution. This work defines and derives a framework for a full 3D tomography of cloud droplets for both their mass concentration in space and their distribution across a range of sizes. This 3D retrieval of key microphysical properties is made tractable by our novel approach that involves a restructuring and differentiation of an open-source polarized 3D RT code to accommodate a special two-step optimization technique. Physically-realistic synthetic clouds are used to demonstrate the methodology with rigorous uncertainty quantification.

Keywords: polarization; 3D radiative transfer; inverse problems; tomography; remote sensing; convective clouds; cloud microphysics

1. Motivation, Context & Outline

Clouds play a significant role at local and global scales, affecting weather, the water cycle, solar power generation, and impacting the Earth's energy balance [1]. Moreover, uncertainties in global climate models are significantly affected by our limited understanding, and therefore modeling, of cloud dynamics and microphysics [2]. Thus, understanding, modeling, and predicting cloud properties is a key issue with worldwide socio-economic implications that is in the center of many research studies [3]. Much of the current understanding relies on routine remote sensing of cloud properties such as by the MODerate resolution Imaging Spectrometer (MODIS) [4]. In practice, global-scale retrievals have so far been based on an individual pixel basis, using an approximation that clouds are plane-parallel slabs. This approximation uses a 1D radiative transfer (RT) model, which leads to biases in many retrievals [5] while other retrievals simply fail [6]. Convective clouds are therefore a blind spot due to their inherently 3D nature.

In its 2018 Decadal Strategy for Earth Observation from Space [7], the National Academies of Sciences, Engineering, and Medicine have indeed identified "Clouds, Convection, and Precipitation" as one of its five top-priority Targeted Variables for NASA's next generation of satellite missions. To bridge this gap, new technology is needed to study clouds as 3D volumetric objects, on a global scale. The *CloudCT* [8] space mission, by the European Research Council (ERC), is specifically destined to provide data and products for this goal. It will involve 10 nano-satellites orbiting in formation, thus acquiring simultaneously unique multi-view measurements of such vertically-developed 3D clouds (Figure 1).

Moreover, common retrieval of cloud droplet characteristics use two optical bands simultaneously [9]: a visible band, where reflected radiance increases with cloud optical thickness, and a shortwave infra-red (SWIR) band, where absorption by condensed water depends on cloud droplet size. To sense droplet size in 3D by CloudCT or other future missions, sensors will need to have either SWIR or polarization capability.

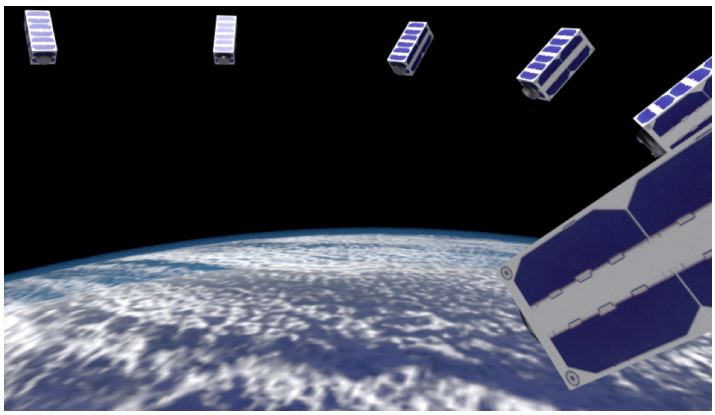

Figure 1. Artist's illustration of the CloudCT [8] mission: a distributed multi-view system of 10 nano-satellites orbiting the Earth in formation. Measurements acquired by the formation will enable tomographic retrievals of cloud properties. Courtesy Mark Sheinin.

1.1. Why Polarized Light?

There is an additional caveat in common retrievals, which rely on SWIR absorption [9]. In addition to absorption, light undergoes multiple scattering in clouds. Multiple scattering diminishes sensitivity to droplet microphysics. High sensitivity to microphysics is embedded in single-scattering events. It is thus beneficial to pick-up single-scatter signals, out of the strong multiply-scattered background radiance. Polarization signals of scattered light are dominated by single-scattering events, and are thus highly sensitive to the type and size specifications of scatters. Polarization therefore provides a significant signal for retrieval of droplet size distributions. In contrast, the intensity signal, which undergoes multiple-scattering events before reaching the sensor, is insensitive to the droplet size and provides complementary information about optical densities within the cloud.

In recent years, there is growing interest in polarimetric imagers for remote sensing of clouds and aerosols [10–16]. In turn, increased interest in polarimetric sensing capabilities has led to the development of 1D and 3D polarized (or "vector") RT codes [17,18] with an aim of improving retrieval algorithms. Motivated by the CloudCT mission formulation—only the first of many to come in innovative passive cloud remote sensing—we develop herein a novel framework for 3D remote sensing of cloud properties using multi-view polarimetric measurements.

1.2. Why Passive Tomography?

From its etymology, the word "tomography" means a slice-by-slice recovery of an object's 3D internal structure using 2D projections of cumulative density. In the computer age, this task is termed Computed Tomography (CT) [19]. Common medical CT approaches are transmission-based X-ray CT

or single-photon emission computed tomography (SPECT). There, 2D projections represent straight line-of-sight (LOS) integrals of the local X-ray opacity or nuclear marker density, respectively. In both imaging modalities, the inverse problem of recovering the medium content is linear [20].

Medical CT modalities generally use active radiation. Active methods are also used for atmospheric sensing or scatterers by radar and lidar. There, a transmitter and receiver are generally collocated and signals are based on backscattering and time-resolved two-way transmission. Probing is solved per LOS using methods which are computationally relatively simple. However, the technology is expensive, horizontal sampling is generally very limited, and irradiance decays fast from the transmitter. Passive sensing is less expensive, uses minimal power, and can image wide swaths of Earth. Thus global coverage mandates passive imaging from space. Consequently, this paper focuses on the derivation of 3D passive tomography of scatterer fields.

In passive imaging of scatterers, the light source irradiating the atmosphere is the sun: uncontrolled, steady and mono-directional. Passive remote sensing does not benefit from pulsed sources for echo-location. It should rely on multi-angular data. In general, however, retrieving atmospheric scatterer fields in 3D requires a full forward model of scattering in 3D. The model generalizes both the direct transmission model of linear CT and the diffusion limit. It can handle atmospheric regimes where neither a direct transmission model nor the diffusion limit are valid.

1.3. Context

In one sense or another, without tomography per se, three-dimensional cloud analysis using remote sensing data has been a topic of research for over two decades. There are well-known biases in optical thickness retrievals using the independent pixel approximation (IPA). To remove these biases, Marshak, et al. [21] invokes an inverse *nonlocal* IPA (NIPA). Marshak et al. [21] further demonstrates this approach on a single realization of a stochastic model for marine stratocumulus (Sc). NIPA is based on the RT Green's function for horizontal (cross-pixel) transport of solar radiation between irradiation and escape to the above-head sensor, which can be computed numerically and conveniently parameterized. Using many instances of the same stochastic cloud model, neural networks (NNs) were successfully trained to retrieve domain-average cloud properties from nadir radiance fields [22–24]. Zinner et al. [25] generalized NIPA to multi-spectral retrievals of both optical thickness and column-averaged effective radius. Iwabuchi and Hayasaka [26] creatively combined NIPA-like physics-based and NN-like statistical regression methods to retrieve spatially varying properties of Sc clouds without suffering from IPA-induced biases.

Multi-angle Imaging Spectro-Radiometer (MISR)/Terra [27] was launched in 1999 and soon inspired research into cloud or cloud field reconstruction based on its unique multi-angle imaging capability. Marchand and Ackerman [28] used the original scalar version of the Spherical Harmonics Discrete Ordinates Method (SHDOM) iteratively to fit MISR observations of marine Sc by modifying the column optical thickness under each pixel. Other early pioneers were Seiz and Davies [29] who reconstructed the outer shell of a 2D transect through a large convective cloud by applying labor-intensive stereographic methods to MISR's multi-angle imagery. Cornet and Davies [30] then estimated the mean optical thickness of that same cloud by performing repeated Monte Carlo 3D RT simulations, holding the outer shape constant, to fit the MISR radiometry. Evans et al. [31] trained a neural network to improve on the IPA retrieval of mean optical depth and its standard deviation using one or more MISR angles. To that effect, these last authors used SHDOM to compute multi-angle radiance fields from very many cloud fields generated with a Large Eddy Simulation (LES). This started a new trend in uncertainty quantification (UQ) in cloud remote sensing, using LES for ground truth that has by now become the standard, and used here as well.

There is a renewed interest in determining a cloud's outer surface in its own right. On the one hand, very high resolution imagery from ground [32] or space [33] has been processed by stereophotogrammetric methods to generate dense "point clouds" representing many features seen from two cameras. On the other hand, the multi-view technique of "space carving"—used here

for initializing the iterative tomography—defines the 3D region that contains a certain cloud by intersecting threshold-based cloud masks from multiple directions. Space carving methods have been applied to determine conservatively the outer shape of clouds observed with the airborne hyperangular Research Spectro-Polarimeter (RSP) [34], MISR [35] (same cloud as Reference [29]), and other sensors (e.g., References [36,37]). Note that methods based on cloud-masking, feature detection-and-tracking and/or stereoscopic location do not require radiometrically calibrated sensors. The loosened radiomeric use seems sub-optimal, since most sensors are in fact painstakingly calibrated to stringent (NIST-traceable) standards. Zinner et al. [38] have, to some extent, reconciled the notion of cloud surface sensing and RT-based cloud property estimation. Their approach scans the illuminated sides of vertically-developed convective clouds using a multispectral sensor mounted on an airborne platform. Then, a standard bi-spectral technique infers the vertical profile of cloud particle size along the side of the cloud. Alexandrov et al. [39] used LES clouds and 3D vector RT to demonstrate cloud-side microphysical profiling with RSP's scanning polarimetric capability.

Remote sensing of clouds in complex 3D scenarios has already benefited from the advent of convolutional neural networks (CNNs), which excel in mapping one or more (e.g., multi-spectral) images, to inherent properties of the objects in the scene. The CNN is trained on a large database where the multi-spectral radiances are simulated with 3D RT and the pixel-scale cloud properties (typically, optical thickness and column-mean effective droplet radius) are known from the LES and assumed microphysics. Deep learning has thus been applied to both nadir satellite imagery [40] and to an array of ground-based sky cameras [41].

To close this non-exhaustive survey of cloud or cloud scene reconstruction techniques, we mention data fusion, which generally involves a combination of active and passive sensors. Liou et al. [42] blazed this path toward the inference of 3D cloud structure by creatively using a combination of ground-based mm-wave radar and multi-spectral imagery from a NOAA satellite overflying the same region. The radar delivers only a vertical 2D "curtain" of radar reflectivities from an extensive cirrus layer, while the multi-spectral imager provides raw information about the horizontal structure of the same cirrus layer. Barker et al. [43] used A-train satellite data (CloudSat, CALISPO, MODIS) to construct a plausible 3D cloud scene by populating off-nadir columns (where actively-probed profiles are lacking) by looking for a sub-satellite (hence actively profiled) pixel that is close in multi-spectral space. This "donor–receiver" algorithm is then iterated until a broadband 3D RT estimation of up-welling flux at the top of the atmosphere (TOA) agrees with the CERES measurement of it, thus satisfying a form of radiative closure. Fielding et al. [44] formalize cloud scene reconstruction with fused ground-based passive/active observations using an ensemble Kalman filter technique. Ensemble Kalman filtering is common in data assimilation for numerical weather prediction. Fielding et al. [44] assimilate observations into a suite of forward models based on 1D or 3D RT, however, rather than into the primitive equations of atmospheric dynamics.

1.4. Outline

Linear CT models (analogous to medical Xray CT and SPECT) were used to study gas emission and absorption in 3D plumes in the vicinity of pollution sources [45,46] or volcanoes [47,48]. There, Rayleigh-scattered sunlight was transmitted through the gas to a spectrometer on a platform flying around the plume. Following the vision of Werner et al. [49], Huang et al. [50,51] used scanning microwave radiometers to reconstruct 2D slices of particle density in clouds based on its impact on local emissivity. Linear CT was also adapted by Garay et al. [52] to characterize a smoke plume over water emanating from a coastal wild fire. There, the signal is sunlight scattered to space and detected by the Multi-angle Imaging Spectro-Radiometer (MISR) sensor [27] at nine viewing angles. The analysis in Reference [52] yields the direct transmission through the plume per LOS, from which linear CT analysis yields the plume density without using solar radiometers under the plume. Aides et al. [53] formulated CT based on single-scattered light. Their forward model is based on sets of broken-ray paths, where light changes direction once from the sun to a sensor. All the above atmospheric

tomography methods assume the medium to be optically thin enough for direct and once-scattered radiation to dominate the measured radiance.

Biomedical imaging also involves CT modalities which are not based on linear models. A notable case in scattering-based tomography of X-ray CT is in Reference [54]. It exploits scattered radiation to obtain reconstruction with significantly lower dose and simpler acquisition hardware relative to linear CT systems, while enhancing estimation of chemical decomposition per volume element. Another example is Optical Diffusion Tomography (ODT) [55–57], which uses non-ionizing near-infrared light. It is worth noting the work by Che et al. [58] which departs from physics-based approaches into the realm of machine learning.

In contrast to ODT and the linear models described, which rely on either very high or very low orders of scattering, we use a steady-state polarized 3D RT forward model which generalizes far beyond these assumptions. This approach can seamlessly extract information about droplet sizes and densities from all orders of scattering.

Specifically, we adopt the vector Spherical Harmonics Discrete Ordinates Method (vSHDOM) [59,60], a popular computational 3D polarized RT model that, importantly here, is open source. We then formulate an inverse 3D RT problem for cloud tomography utilizing multi-view multi-spectral polarimetric images. In contrast to linear CT, the image formation model is nonlinear in the cloud's microphysical and density variables. Our approach seeks an optimal fit of observed data to a physical model based on droplet microphysical and density parameters. Our work here generalizes our prior inversion approaches, which have been based on intensity-only observations [61–65]. Our generalization takes advantage of polarimetric measurements, thereby providing the benefits described in Section 1.1.

In Section 2, we cover basic cloud droplet optics using Mie scattering theory and the fundamentals of polarized 3D RT. The latter yields radiance which has a clear decomposition into single- and multiply-scattered light. This decomposition supports the solution to the inverse problem at hand. We then lay out our 3D cloud tomography method where we target three basic microphysical properties, volumetrically. Necessary but tedious mathematical details are presented in the Appendix A. Subsequently, the new 3D cloud tomographic capability is demonstrated on realistic synthetic clouds from an LES that provide ground truth for unambiguous retrieval error quantification. We conclude with a summary of our results and an outline of future developments, mostly looking toward CloudCT and other future space-based uses.

2. Theoretical Background

This section describes bulk microphysical parameterization of scattering media, the polarimetric radiative transfer image formation (forward) model and the relation between them. The section also describes the coordinate systems in use (per-scatterer, imager and Earth frames). We further decompose the polarized radiance into single-scattered and high-order scattered components. These foundations are used in subsequent sections, to formulate tomographic recovery. For concise reading, this section does not elaborate on some definitions. An extended, self-contained theoretical background section is given in Appendix A, which the readers are encouraged to follow to ease reproduction of our results.

2.1. Scatterer Microphysical Properties

In the lower atmosphere, cloud particles are droplets of liquid water that are very nearly spherical, having radius r. They are however polydisperse, with a droplet size distribution denoted $n(r)$. For most remote-sensing purposes, $n(r)$ is parameterized using an *effective radius*, r_{e} (in μm) and a dimensionless *variance*, v_{e} [66]. A commonly used parametric size distribution with empirical support [66] is the *Gamma*-distribution (Figure 2), detailed in Appendix A.1. Let ρ_{w} be the density of liquid water. An important cloud characteristic is the water mass density or Liquid Water Content (LWC) per unit volume. The parameters r_{e} and v_{e} dictate the shape of the droplet size distribution.

LWC relates to droplet size and concentration, thus to optical opacity. In Section 3 the parameters LWC, r_e, v_e are unknown quantities, which we seek to estimate on a 3D grid.

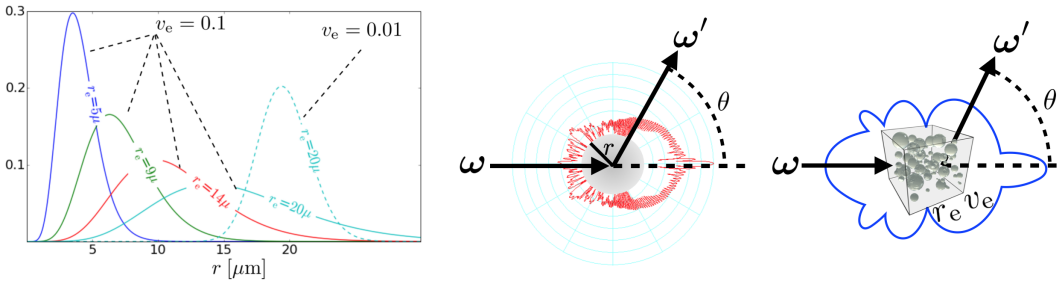

Figure 2. (**Left**) A Normalized *Gamma* droplet size distribution. The effective radius and variance dictate the centroid and width of the droplet size distribution. The limit of very low v_e approaches a mono-disperse distribution. (**Center**) Log-polar plot of the Mie phase-function p_{11} induced by a single water sphere of radius r. (**Right**) Log-polar plot of the effective phase-function $\langle s_s p_{11} \rangle_r / \sigma_s$ induced by a small volume that includes particles of different sizes.

2.2. Single Scattering of Polarized Light

In the absence of molecular absorption, material optical properties can be approximated using a single wavelength for each spectral band. This approximation, commonly used in multi-spectral remote sensing, relies on a single rendering of spectrally-averaged optical properties. It is valid if wavelength dependencies within a spectral band are weak, a condition met when narrow bands are considered. Macroscopic optical cross-sections are then expressed as averages weighted by the size-distribution $n(r)$. We respectively denote the extinction, scattering and absorption cross-sections as

$$\sigma_t(\lambda),\ \sigma_s(\lambda),\ \sigma_a(\lambda). \tag{1}$$

Note that throughout the text, dependency on λ is generally omitted for simplicity; however, it is used at specific points as needed.

Scattering, as a fraction of the overall interaction [67], is expressed by the dimensionless single scattering albedo

$$\varpi = \frac{\sigma_s}{\sigma_t}. \tag{2}$$

The extinction coefficient (or optical density), denoted by β, is expressed in terms of the LWC as [68]

$$\beta = \mathrm{LWC} \cdot \tilde{\sigma}_t. \tag{3}$$

Here, $\tilde{\sigma}_t$ is the mass extinction coefficient (in units of m^2/g).

Let $\boldsymbol{\omega}$ and $\boldsymbol{\omega}'$ be the unitary incident and scattered ray direction vectors respectively in Figure 2. Single-scattering geometry is defined by the local coordinate system of the incoming beam's electric fields. The electric field of incoming light is decomposed into components along orthogonal directions. We set them as

$$\mathbf{E}_1 \propto \boldsymbol{\omega} \times \boldsymbol{\omega}', \quad \mathbf{E}_2 \propto \mathbf{E}_1 \times \boldsymbol{\omega}. \tag{4}$$

The scattering angle is $\theta = \cos^{-1}(\boldsymbol{\omega}\cdot\boldsymbol{\omega}')$. The angular redistribution of singly-scatterred light by a volume element is defined by the macroscopic *phase matrix* $\mathbf{P}(\theta)$. For spherical (or just randomly-oriented) particles, the phase-matrix $\mathbf{P}(\theta)$ takes the following symmetric form [66]

$$\mathbf{P}(\theta) = \begin{bmatrix} p_{11}(\theta) & p_{21}(\theta) & 0 & 0 \\ p_{21}(\theta) & p_{22}(\theta) & 0 & 0 \\ 0 & 0 & p_{33}(\theta) & -p_{43}(\theta) \\ 0 & 0 & p_{43}(\theta) & p_{44}(\theta) \end{bmatrix}, \tag{5}$$

where p_{11} is the (unpolarized) scattering phase-function.

It is convenient to define the state of polarized light in terms of the Stokes [66] vector $\mathbf{I} = (I, Q, U, V)^\top$, where I is the unpolarized intensity. The Stokes components relate to statistics of the fields $\mathbf{E}_1, \mathbf{E}_2$ mentioned in Equation (4), as described in Appendix A.2. The degrees of polarization (DOP) and linear polarization (DoLP) are respectively defined as the ratios $\sqrt{Q^2+U^2+V^2}/I$, $\sqrt{Q^2+U^2}/I$. The angle of linear polarization (AoLP) is $1/2\,\tan^{-1}(U/Q)$. Referring to the matrix elements in Equation (5), in single-scattering of unpolarized incident sunlight, the DoLP of scattered light amounts to the ratio $|p_{21}|/p_{11}$.

Mie Scattering

Mie theory describes how light interacts with a spherical particle of size comparable to λ [69]. Denote $\mu = \cos\theta$. Scattering of the Stokes vector $\mathbf{I}$ is described by the phase matrix $\mathbf{P}_{\text{Mie}}(\mu)$, which is fully defined by six matrix components:

$$p_{11}^{\text{Mie}}(\mu),\ p_{12}^{\text{Mie}}(\mu),\ p_{22}^{\text{Mie}}(\mu),\ p_{33}^{\text{Mie}}(\mu),\ p_{43}^{\text{Mie}}(\mu),\ p_{44}^{\text{Mie}}(\mu). \tag{6}$$

Expressions of Mie and Rayleigh scattering phase matrices are given in Appendix A.3.

Mie scattering due to water droplets peaks at specific angles. For a single droplet or monodisperse material, $\mathbf{P}^{\text{Mie}}$ has sharp scattering lobes at angles that depend on the droplet's r/λ ratio. A macroscopic voxel contains droplets in a range of radii r, smoothing the scattering lobes. The smoothing effect depends on v_{e} (Figure 3). Two angular domains that stand out for remote-sensing purposes are the cloud-bow ($\theta \in [135°, 155°]$) and glory ($\theta \in [175°, 180°]$). Both domains have peaks that are sensitive to the droplet microphysical parameters, and are significantly polarized (i.e., peaks are visible in the p_{12}^{Mie} component). The latter fact renders these peaks distinguishable in the presence of a multiply-scattered signal component.

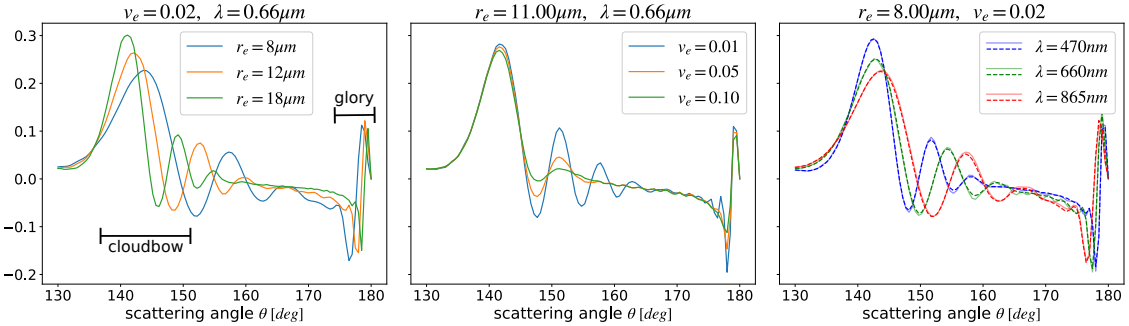

Figure 3. Normalized phase matrix element $-p_{12}^{\text{Mie}}/p_{11}^{\text{Mie}}$ around the cloud-bow and glory regions. For highly disperse droplet distributions (large v_e) the secondary lobes of the cloud-bow ($\theta \sim 140°$) and glory ($\theta \sim 180°$) diminish. The main cloud-bow peak is slightly sensitive to λ or v_{e}. The side-lobe angles are more sensitive to λ and r_{e}. The side-lobe amplitude is sensitive to v_{e}. This cloud-bow signal is helpful for retrievals of r_{e}. [Right plot] Solid lines indicate monochromatic light. Dashed lines indicate spectral averaging over a 100 nm bandwidth, which is more than double any of the spectral bands considered further on.

2.3. Multiple Scattering of Polarized Light

The *Radiative Transfer Equation* (RTE) [70] describes multiple scattering interactions of monochromatic partially polarized light within a medium. Transmittance between two points $\boldsymbol{x}_1, \boldsymbol{x}_2$ is

$$T\left(\boldsymbol{x}_1 \rightarrow \boldsymbol{x}_2\right) = \exp\left[-\int_{\boldsymbol{x}_1}^{\boldsymbol{x}_2} \beta(\boldsymbol{x}) \mathrm{d}\boldsymbol{x}\right]. \tag{7}$$

An atmospheric domain Ω is bounded by $\partial\Omega$. The intersection of $\partial\Omega$ with a ray originating at point $\boldsymbol{x}$ in direction $-\boldsymbol{\omega}$ (Figure 4) is denoted $\boldsymbol{x}_0(\boldsymbol{x}, \boldsymbol{\omega})$. Denote the Stokes vector field as $\mathbf{I}\left(\boldsymbol{x}, \boldsymbol{\omega}\right)$. Then $\mathbf{I}(\boldsymbol{x}_0, \boldsymbol{\omega})$ is the Stokes vector of radiation which propagates in direction $\boldsymbol{\omega}$ at boundary point $\boldsymbol{x}_0(\boldsymbol{x}, \boldsymbol{\omega})$. The non-emissive forward RT model [70] couples $\mathbf{I}\left(\boldsymbol{x}, \boldsymbol{\omega}\right)$ to a vector *source field* $\mathbf{J}\left(\boldsymbol{x}, \boldsymbol{\omega}\right)$ (Figure 4) by

$$\mathbf{I}\left(\boldsymbol{x}, \boldsymbol{\omega}\right) = \mathbf{I}(\boldsymbol{x}_0, \boldsymbol{\omega}) T\left(\boldsymbol{x}_0 \rightarrow \boldsymbol{x}\right) + \int_{\boldsymbol{x}_0}^{\boldsymbol{x}} \mathbf{J}(\boldsymbol{x}', \boldsymbol{\omega}) \beta(\boldsymbol{x}') T\left(\boldsymbol{x}' \rightarrow \boldsymbol{x}\right) \mathrm{d}\boldsymbol{x}', \tag{8}$$

$$\mathbf{J}\left(\boldsymbol{x}, \boldsymbol{\omega}\right) = \frac{\varpi(\boldsymbol{x})}{4\pi} \int_{4\pi} \mathbf{P}\left(\boldsymbol{x}, \boldsymbol{\omega} \cdot \boldsymbol{\omega}'\right) \mathbf{I}\left(\boldsymbol{x}, \boldsymbol{\omega}'\right) \mathrm{d}\boldsymbol{\omega}'. \tag{9}$$

Equations (8)–(9) are solved numerically, either directly with an explicit solver [60] or indirectly using a Monte-Carlo path tracer [71]. We use vSHDOM [60] to simulate scattered Stokes components of a realistic atmosphere, having both Mie and Rayleigh scattering due to water droplets and air molecules.

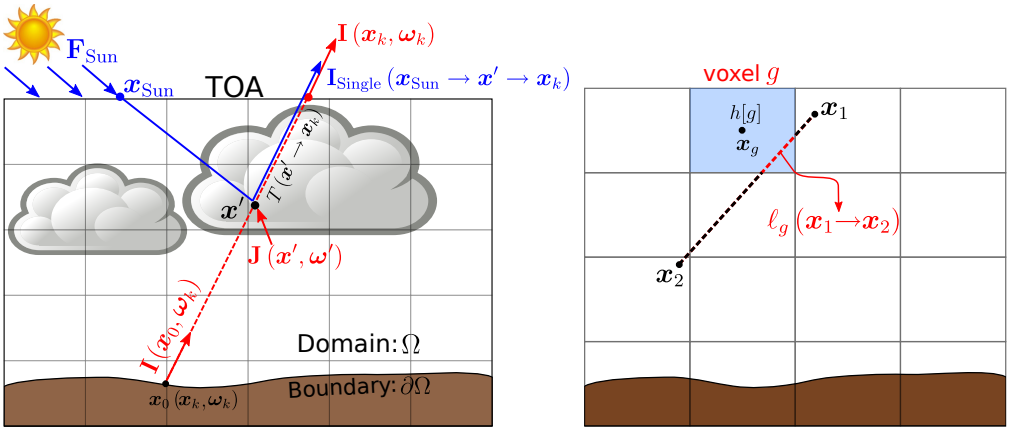

Figure 4. (**Left**) Light scatters in the medium, generally multiple times, creating a partially polarized (vector) scatter field $\mathbf{J}$ (9). Integration yields the partially polarized (vector) light field $\mathbf{I}$ (8). Here $I(\boldsymbol{x}_k, \boldsymbol{\omega}_k)$ is a pixel measurement at the top of the atmosphere (TOA) and $\mathbf{I}_{\text{Single}}$ is the single-scattered contribution from $\boldsymbol{x}'$. (**Right**) Ray tracing of a line-integral over a discretized voxel field $h[g]$ (zero-order interpolation).

Multiple scattering interactions are defined using two coordinate systems. Local *scatterer coordinates* are set by $(\hat{\mathbf{E}}_1, \hat{\mathbf{E}}_2)$. Stokes measurements in satellites, however, are defined in *Meridional* coordinates. Let $\hat{\mathbf{z}}$ denote the zenith direction vector at every point on Earth. In meridian coordinates, the electric field components are defined by direction vectors

$$\hat{\mathbf{m}}_1 = \frac{\hat{\mathbf{z}} \times \boldsymbol{\omega}}{\|\hat{\mathbf{z}} \times \boldsymbol{\omega}\|}, \quad \hat{\mathbf{m}}_2 = \boldsymbol{\omega} \times \hat{\mathbf{m}}_1. \tag{10}$$

Each pixel-scale Stokes measurement is described by a coordinate system defined by $\hat{\mathbf{m}}_1$ and $\hat{\mathbf{m}}_2$. The transformation between the two coordinate systems amounts to a multiplication of $\mathbf{I}$ by a Mueller rotation matrix.

Sampling $\mathbf{I}(\boldsymbol{x}, \boldsymbol{\omega})$ at the location of each camera and direction of each camera pixel yields the measured Stokes vector. A measurement k is taken at the camera position $\boldsymbol{x}_k$, LOS direction $\boldsymbol{\omega}_k$, and wavelength λ_k (Figure 4). Thus, Equations (8) and (9) yield the pixel measurement model

$$\mathbf{I}[k] = \mathbf{I}(\boldsymbol{x}_0, \boldsymbol{\omega}_k)\, T(\boldsymbol{x}_0 \to \boldsymbol{x}_k) + \int_{\boldsymbol{x}_0}^{\boldsymbol{x}_k} \mathbf{J}(\boldsymbol{x}', \boldsymbol{\omega}_k)\, \beta(\boldsymbol{x}') T(\boldsymbol{x}' \to \boldsymbol{x}_k)\, \mathrm{d}\boldsymbol{x}'. \tag{11}$$

2.4. Single-Scattering Separation

It is often convenient to separate the single-scattering contribution from the rest of the radiance field [72]. The solar irradiance at the top of the atmosphere (TOA) is F_{Sun}. It is unoplarized, thus corresponds to a Stokes vector $\mathbf{F}_{\mathrm{Sun}} = (F_{\mathrm{Sun}},\ 0,\ 0,\ 0)^{\top}$. The Sun is modeled as an ideal directional source with direction $\boldsymbol{\omega}_{\mathrm{Sun}}$. A solar ray heading to point $\boldsymbol{x}$ intersects the TOA at point $\boldsymbol{x}_{\mathrm{Sun}}$. The solar transmittance is given by $T(\boldsymbol{x}_{\mathrm{Sun}} \to \boldsymbol{x})$. Let δ denote *Dirac's delta*. Thus, $\mathbf{I}$ can be written as a sum of the *diffuse* component $\mathbf{I}_{\mathrm{d}}$, and direct solar component:

$$\mathbf{I}(\boldsymbol{x}, \boldsymbol{\omega}) = \mathbf{I}_{\mathrm{d}}(\boldsymbol{x}, \boldsymbol{\omega}) + \delta(\boldsymbol{\omega} - \boldsymbol{\omega}_{\mathrm{Sun}})\, \mathbf{F}_{\mathrm{Sun}} T(\boldsymbol{x}_{\mathrm{Sun}} \to \boldsymbol{x}). \tag{12}$$

Inserting (12) into (9) yields

$$\mathbf{J}(\boldsymbol{x}, \boldsymbol{\omega}) = \mathbf{J}_{\mathrm{d}}(\boldsymbol{x}, \boldsymbol{\omega}) + \frac{\varpi(\boldsymbol{x})}{4\pi} \mathbf{P}(\boldsymbol{x}, \boldsymbol{\omega} \cdot \boldsymbol{\omega}_{\mathrm{Sun}})\, \mathbf{F}_{\mathrm{Sun}} T(\boldsymbol{x}_{\mathrm{Sun}} \to \boldsymbol{x}), \tag{13}$$

where

$$\mathbf{J}_{\mathrm{d}}(\boldsymbol{x}, \boldsymbol{\omega}) = \frac{\varpi(\boldsymbol{x})}{4\pi} \int_{4\pi} \mathbf{P}(\boldsymbol{x}, \boldsymbol{\omega} \cdot \boldsymbol{\omega}')\, \mathbf{I}_{\mathrm{d}}(\boldsymbol{x}, \boldsymbol{\omega}')\, \mathrm{d}\boldsymbol{\omega}'. \tag{14}$$

Consider Figure 4. It shows a *broken-ray* path of direct sunlight, which undergoes single scattering at $\boldsymbol{x}'$, then reaches the camera at $\boldsymbol{x}_k$. Denote this broken ray by

$$\boldsymbol{x}_{\mathrm{Sun}} \to \boldsymbol{x}' \to \boldsymbol{x}_k. \tag{15}$$

The direction vector between $\boldsymbol{x}'$ and $\boldsymbol{x}_k$ is $\boldsymbol{\omega}_k$. This broken ray projects to a pixel corresponding to $\boldsymbol{\omega}_k$ at camera location $\boldsymbol{x}_k$ thus contributing to the measurement $\mathbf{I}(\boldsymbol{x}_k, \boldsymbol{\omega}_k)$. Using Equations (8) and (13), the single-scattered contribution from $\boldsymbol{x}'$ is

$$\mathbf{I}_{\mathrm{Single}}(\boldsymbol{x}_{\mathrm{Sun}} \to \boldsymbol{x}' \to \boldsymbol{x}_k) = \frac{\varpi(\boldsymbol{x}')}{4\pi} \beta(\boldsymbol{x}') \mathbf{P}(\boldsymbol{x}', \boldsymbol{\omega}_k \cdot \boldsymbol{\omega}_{\mathrm{Sun}})\, \mathbf{F}_{\mathrm{Sun}} T(\boldsymbol{x}_{\mathrm{Sun}} \to \boldsymbol{x}')\, T(\boldsymbol{x}' \to \boldsymbol{x}_k). \tag{16}$$

Thus, the entire single-scattered signal accumulates contributions along the LOS

$$\mathbf{I}_{\mathrm{Single}}(\boldsymbol{x}_k) = \int_{\boldsymbol{x}_0}^{\boldsymbol{x}_k} \mathbf{I}_{\mathrm{Single}}(\boldsymbol{x}_{\mathrm{Sun}} \to \boldsymbol{x}' \to \boldsymbol{x}_k)\, \mathrm{d}\boldsymbol{x}'. \tag{17}$$

2.5. Ray Tracing

Ray tracing computes a function over a straight line through a 3D domain. A common operation is path-integration (e.g., Equations (7) and (8)). Let $h(\boldsymbol{x})$ be a continuous field. Define a grid of discrete points $\boldsymbol{x}_g$, where $g = 1, 2, ..., N_{\mathrm{grid}}$. Denote $h[g] = h(\boldsymbol{x}_g)$. A path-integral over $h(\boldsymbol{x})$ is numerically computed using an interpolation kernel K

$$\int_{\boldsymbol{x}_1}^{\boldsymbol{x}_2} h(\boldsymbol{x}) \mathrm{d}\boldsymbol{x} = \sum_{g=1}^{N_{\mathrm{grid}}} h[g] \int_{\boldsymbol{x}_1}^{\boldsymbol{x}_2} K(\boldsymbol{x} - \boldsymbol{x}_g)\, \mathrm{d}\boldsymbol{x}. \tag{18}$$

For zero-order interpolation (i.e., voxel grid), (18) degenerates to

$$\int_{\boldsymbol{x}_1}^{\boldsymbol{x}_2} h(\boldsymbol{x})\mathrm{d}\boldsymbol{x} = \sum_{g=1}^{N_{\mathrm{grid}}} h[g]\ell_g\left(\boldsymbol{x}_1 \rightarrow \boldsymbol{x}_2\right), \tag{19}$$

where $\ell_g\left(\boldsymbol{x}_1 \rightarrow \boldsymbol{x}_2\right)$ is the intersection of the path with voxel g (Figure 4). For voxel indices g that do not intersect the path $\boldsymbol{x}_1 \rightarrow \boldsymbol{x}_2$, the value of $\ell_g\left(\boldsymbol{x}_1 \rightarrow \boldsymbol{x}_2\right)$ is 0.

3. Cloud Tomography

So far, we described the forward (image-formation) model, that is, how images are formed, given cloud properties. In this work, we formulate a novel inverse tomographic problem of recovering the unknown cloud microphysical properties, volumetrically. In voxel g, the vector of unknown parameters is $(\mathrm{LWC}[g],\ r_{\mathrm{e}}[g],\ v_{\mathrm{e}}[g])$. The unknown microphysical parameters are concatenated to a vector of length $3N_{\mathrm{grid}}$

$$\Theta = \left(..., \mathrm{LWC}[g],\ r_{\mathrm{e}}[g],\ v_{\mathrm{e}}[g], ...\right)^{\top}, \quad 1 \leq g \leq N_{\mathrm{grid}}. \tag{20}$$

Neglecting circular polarization, each pixel measures a Stokes vector, $\mathbf{y_I} = \left(y_{\mathrm{I}}, y_{\mathrm{Q}}, y_{\mathrm{U}}\right)$ at N_λ wavelengths. Let N_{views} and N_{pix} denote the number of view points and camera pixels. The total number of Stokes measurements is thus $N_{\mathrm{meas}}{=}N_\lambda N_{\mathrm{views}} N_{\mathrm{pix}}$. The measurement vector of length $3N_{\mathrm{meas}}$ is expressed as

$$\mathbf{y} = \left(\mathbf{y_I}[1], ..., \mathbf{y_I}[N_{\mathrm{meas}}]\right)^{\top}. \tag{21}$$

In this section, we formulate the use of measurements $\mathbf{y}$ (multi-view, multi-pixel, multi-spectral, polarimetric measurements) for tomographic retrieval of Θ (3D volumetric cloud density and microphysics). It is worth mentioning at this point that the Stokes components are not measured directly. Rather, they are computationally retrieved from measurements taken using different states of polarization filters (see Appendix C for the AirMSPI measurement model).

3.1. Polarimetric Information

To make an initial assessment of the sensitivity of polarimetric measurements, we simulate a simple homogeneous cubic cloud (Figure 5), parameterized by two microphysical parameters: $(\mathrm{LWC}, r_{\mathrm{e}})$. Back-scattered Stokes measurements are taken at the TOA for the same angles and wavelengths as sampled by the Airborne Multi-angle Spectro-Polarimetric Imager (AirMSPI) [14]. AirMSPI is used here as a *proxy instrument* to demonstrate our approach. However, the approach is applicable to other polarimetric imagers.

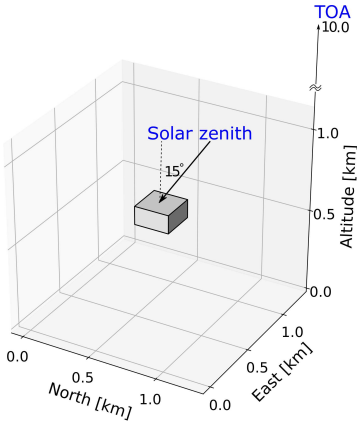

Figure 5. A homogeneous cubic cloud illuminated with solar radiation at a zenith angle of 15° off-nadir. The solar azimuth angles are $\phi_0 = [0.0°, 67.5°]$. The outgoing Stokes vector $\mathbf{I}$ is simulated at AirMSPI resolution and wavelengths, with AirMSPI measuring along a North-bound track.

Let $I[k], U[k], Q[k]$ be simulated Stokes components at measurement index k, and let v_e be held constant. Define a cost (data-misfit) function for each of the Stokes components

$$\mathcal{D}_\mathrm{I}\left(\mathrm{LWC}, r_\mathrm{e}\right) = \sum_{k=1}^{N_\mathrm{meas}} \left(I[k] - y_\mathrm{I}[k]\right)^2, \tag{22}$$

$$\mathcal{D}_\mathrm{Q}\left(\mathrm{LWC}, r_\mathrm{e}\right) = \sum_{k=1}^{N_\mathrm{meas}} \left(Q[k] - y_\mathrm{Q}[k]\right)^2, \tag{23}$$

$$\mathcal{D}_\mathrm{U}\left(\mathrm{LWC}, r_\mathrm{e}\right) = \sum_{k=1}^{N_\mathrm{meas}} \left(U[k] - y_\mathrm{U}[k]\right)^2. \tag{24}$$

Equations (22)–(24) are 2D manifolds. Figure 6 plots the cost manifolds for different solar azimuth angles, ϕ_0. While there is an ambiguity between LWC and r_e when relying on $\mathcal{D}_\mathrm{I}$, there are better defined minima for $\mathcal{D}_\mathrm{Q}$ and $\mathcal{D}_\mathrm{U}$. This indicates that polarization measurements carry valuable information.

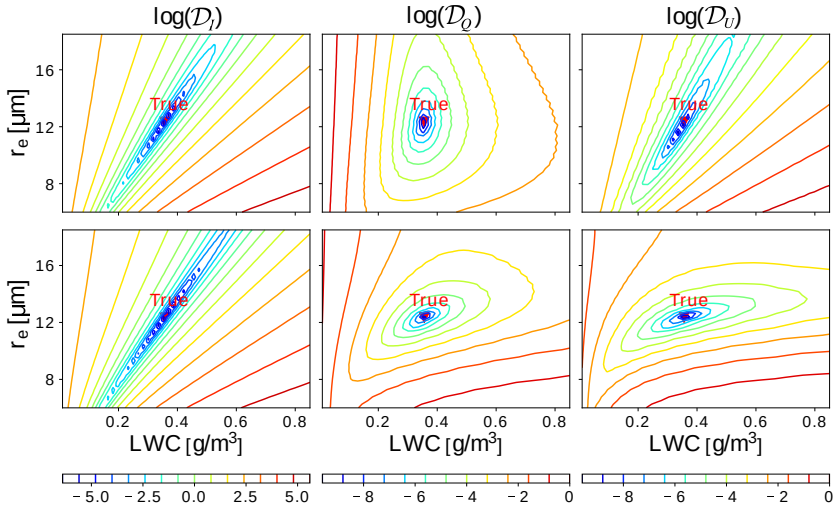

Figure 6. Logarithm of the 2D cost manifolds for a 2-parameter homogeneous cubic cloud (Figure 5). Each column of plots corresponds to the cost of the different Stokes components in Equations (22)–(24). Each row of plots corresponds to a different Solar azimuth angle ϕ_0.

3.2. Inverse Problem Formulation

Denote $\mathbf{I}_\Theta$ as the image formation model. Tomography can be formulated as minimization of a data-fit function. We perform

$$\hat{\Theta} = \arg\min_{\Theta} \mathcal{D}\left(\mathbf{I}_\Theta, \mathbf{y}\right) = \arg\min_{\Theta} \left(\mathbf{I}_\Theta - \mathbf{y}\right)^\top \Sigma^{-1} \left(\mathbf{I}_\Theta - \mathbf{y}\right), \tag{25}$$

Here Σ is related to the co-variance matrix of the measurement noise. For brevity, we omit the subscript Θ but remember that

$$\mathbf{I} \equiv \mathbf{I}_\Theta, \;\; \mathbf{J} \equiv \mathbf{J}_\Theta, \;\; \beta \equiv \beta_\Theta, \;\; \varpi \equiv \varpi_\Theta, \;\; \mathbf{P} \equiv \mathbf{P}_\Theta, \;\; T \equiv T_\Theta. \tag{26}$$

Assuming noise in different pixels, wavelengths and angles is uncorrelated, (25) degenerates to

$$\hat{\Theta} = \arg\min_{\Theta} \sum_{k=1}^{N_{\text{meas}}} \left(\mathbf{I}[k] - \mathbf{y}_\mathbf{I}[k]\right)^\top \mathbf{R}^{-1} \left(\mathbf{I}[k] - \mathbf{y}_\mathbf{I}[k]\right). \tag{27}$$

The matrix $\mathbf{R}$ depends on the particular sensor technology. Description of $\mathbf{R}$, tailored to the AirMSPI sensor, is detailed in Appendix C.

We solve (27) by a gradient-based approach. The gradient with respect to the unknown parameters Θ is

$$\nabla_\Theta \mathcal{D}\left(\mathbf{I}_\Theta, \mathbf{y}\right) = 2 \sum_{k=1}^{N_{\text{meas}}} \left(\mathbf{I}[k] - \mathbf{y}_\mathbf{I}[k]\right)^\top \mathbf{R}^{-1} \nabla_\Theta \mathbf{I}[k]. \tag{28}$$

The term $\nabla_\Theta \mathbf{I}[k]$ is the *Jacobian* of the sensing model. Equation (28) is used to formulate an update rule for an iterative optimization algorithm

$$\Theta_{b+1} = \Theta_b - \chi_b \nabla_\Theta \mathcal{D}\left(\mathbf{I}_\Theta, \mathbf{y}\right), \tag{29}$$

where b denotes the iteration index and χ_b is a scalar. We use L-BFGS [73] for numerical optimization that, in particular, determines the value of χ_b adaptively. One approach to computing the gradient $\nabla_\Theta \mathcal{D}$ is the *Adjoint RTE* [74,75]. Due to the recursive nature of the RTE, computing the gradient through the exact Jacobian $\nabla_\Theta \mathbf{I}[k]$ is computationally expensive. In the following sections, we derive a method to make the computation of the gradient tractable and efficient. We do that by approximating the Jacobian $\nabla_\Theta \mathbf{I}$ in a tractable way, using a two-step iterative algorithm [61,63].

3.3. Iterative Solution Approach

We formulate an iterative algorithm which alternates between two steps (See the diagram in Figure 7).

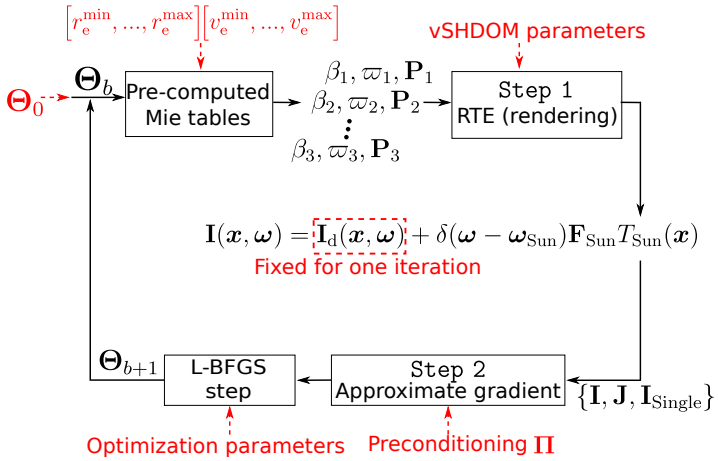

Figure 7. A block diagram of the iterative algorithm. Red marks hyper-parameters. Numerical parameters of vector Spherical Harmonics Discrete Ordinates Method (vSHDOM) and L-BFGS are summarized in Appendix D (Table A2).

Starting with an initial guess, Θ_0, `Step 1` uses vSHDOM to compute the forward (recursive) RT equations. This renders synthetic images according to the multi-view geometry, spectral bands and spatial samples of the cameras. Keeping $\mathbf{I}_d$ fixed, `Step 2` efficiently computes an approximate gradient with respect to Θ. The approximate gradient is fed into an L-BFGS step to update the current estimate Θ_b.

`Step 1: RTE Forward Model`

The first step in the estimation approach is running the forward model in Equations (8) and (9) using a numerical RTE solver. This requires transforming microphysical to optical properties at every voxel (g) and spectral band (λ):

$$\text{LWC}[g],\ r_e[g],\ v_e[g] \longrightarrow \beta_\lambda[g],\ \varpi_\lambda[g],\ \mathbf{P}_\lambda[g]. \tag{30}$$

This transformation can be implemented as described in Appendix A, using specifically Equations (A8)–(A13). However, using this implementation during each optimization iteration can be time-consuming. Therefore, we use pre-computed lookup tables, $\tilde{\sigma}_\lambda(r_e, v_e)$, $\varpi_\lambda(r_e, v_e)$, $\mathbf{P}_\lambda(r_e, v_e)$, over the grids $r_e \in [r_e^{min}, ..., r_e^{max}]$ and $v_e \in [v_e^{min}, ..., v_e^{max}]$. With these pre-computed tables and $\{\text{LWC}[g], r_e[g], v_e[g]\}$, vSHDOM [60] renders the Stokes vector at each 3D voxel and direction. This is the forward modeling procedure. The result is the set of fields $\mathbf{I}(\boldsymbol{x}, \boldsymbol{\omega})$, $\mathbf{I}_d(\boldsymbol{x}, \boldsymbol{\omega})$, $\mathbf{J}(\boldsymbol{x}, \boldsymbol{\omega})$, $\mathbf{I}_{Single}(\boldsymbol{x}_{Sun} \rightarrow \boldsymbol{x}' \rightarrow \boldsymbol{x}_k)$.

`Step 2: Approximate Jacobian Computation`

The forward vRTE model in (11) depends on optical properties $(\beta, \varpi, \mathbf{P})$, which themselves depend on the sought microphysics. The Jacobian at voxel g is expressed by applying the chain-rule to (11). For example, the derivative with respect to the effective radius is

$$\frac{\partial \mathbf{I}[k]}{\partial r_e[g]} = \frac{\partial \mathbf{I}[k]}{\partial \beta[g]} \frac{\partial \beta[g]}{\partial r_e[g]} + \frac{\partial \mathbf{I}[k]}{\partial \varpi[g]} \frac{\partial \varpi[g]}{\partial r_e[g]} + \frac{\partial \mathbf{I}[k]}{\partial \mathbf{P}[g]} \frac{\partial \mathbf{P}[g]}{\partial r_e[g]}. \tag{31}$$

Analogously, replacing r_e in (31) with LWC or v_e yields the respective microphysical derivatives. We proceed by expressing the derivatives $\partial\{\beta, \varpi, \mathbf{P}\}/\partial\{\text{LWC}, r_e, v_e\}$. Afterwards, we expand and combine the derivatives $\partial \mathbf{I}/\partial\{\beta, \varpi, \mathbf{P}\}$ to express (31).

For each voxel, the derivatives of $(\beta, \varpi, \mathbf{P})$ with respect to the microphysics are calculated using pre-computed tables

$$\frac{\partial \beta}{\partial \mathrm{LWC}} = \tilde{\sigma}(r_\mathrm{e}, v_\mathrm{e}), \quad \frac{\partial \beta}{\partial r_\mathrm{e}} = \frac{\tilde{\sigma}(r_\mathrm{e}+\varepsilon_{r_\mathrm{e}}, v_\mathrm{e}) - \tilde{\sigma}(r_\mathrm{e}, v_\mathrm{e})}{\varepsilon_{r_\mathrm{e}}}, \tag{32}$$

$$\frac{\partial \varpi}{\partial \mathrm{LWC}} = 0, \quad \frac{\partial \varpi}{\partial r_\mathrm{e}} = \frac{\varpi(r_\mathrm{e}+\varepsilon_{r_\mathrm{e}}, v_\mathrm{e}) - \varpi(r_\mathrm{e}, v_\mathrm{e})}{\varepsilon_{r_\mathrm{e}}}, \tag{33}$$

$$\frac{\partial \mathbf{P}}{\partial \mathrm{LWC}} = 0, \quad \frac{\partial \mathbf{P}}{\partial r_\mathrm{e}} = \frac{\mathbf{P}(r_\mathrm{e}+\varepsilon_{r_\mathrm{e}}, v_\mathrm{e}) - \mathbf{P}(r_\mathrm{e}, v_\mathrm{e})}{\varepsilon_{r_\mathrm{e}}}, \tag{34}$$

where v_e derivatives are computed analogously to the r_e derivatives. Using the shorthand notation $\partial_g \equiv \{\frac{\partial}{\partial \mathrm{LWC}[g]}, \frac{\partial}{\partial r_\mathrm{e}[g]}, \frac{\partial}{\partial v_\mathrm{e}[g]}\}$, the overall Jacobian is given by a sum of terms

$$\partial_g \mathbf{I}[k] = A_1 + A_2 + A_3 + A_4 + A_5 + A_6. \tag{35}$$

The full expression for each term in Equation (35) is given in Appendix B. For example,

$$A_1 = -\ell_g\left(\boldsymbol{x}_0 \rightarrow \boldsymbol{x}_k\right) \mathbf{I}\left(\boldsymbol{x}_0, \boldsymbol{\omega}_k\right) T\left(\boldsymbol{x}_0 \rightarrow \boldsymbol{x}_k\right) \left[\partial_g \beta\right]. \tag{36}$$

Let us focus on the term

$$A_4 = \int_{x_0}^{x_k} \left\{ \frac{\varpi(\boldsymbol{x}')}{4\pi} \int_{4\pi} \mathbf{P}\left(\boldsymbol{x}', \boldsymbol{\omega}_k \cdot \boldsymbol{\omega}'\right) \left[\partial_g \mathbf{I}\left(\boldsymbol{x}', \boldsymbol{\omega}'\right)\right] \mathrm{d}\boldsymbol{\omega}' \right\} \beta(\boldsymbol{x}') T\left(\boldsymbol{x}' \rightarrow \boldsymbol{x}_k\right) \mathrm{d}\boldsymbol{x}'. \tag{37}$$

This Jacobian term stands out, because it is the only term which requires computing the derivative of $\mathbf{I}$. This derivative is computationally expensive because $\mathbf{I}$ is computed recursively through the RTE (Equations (8) and (9)). In principle, a change in the microphysics of one voxel can recursively affect the radiance at every other voxel. We decompose $\partial_g \mathbf{I}$ using the diffuse-direct decomposition of (12)

$$\partial_g \mathbf{I}\left(\boldsymbol{x}', \boldsymbol{\omega}'\right) = \partial_g \mathbf{I}_\mathrm{d}\left(\boldsymbol{x}', \boldsymbol{\omega}'\right) + \delta\left(\boldsymbol{\omega}' - \boldsymbol{\omega}_\mathrm{Sun}\right) \mathbf{F}_\mathrm{Sun} \left[\partial_g T\left(\boldsymbol{x}_\mathrm{Sun} \rightarrow \boldsymbol{x}'\right)\right]. \tag{38}$$

At the core our approach for computational efficiency is the assumption that the diffuse light $\mathbf{I}_\mathrm{d}$ is less sensitive to slight changes in the microphysical properties of any single voxel g. Rather, $\mathbf{I}_\mathrm{d}$ is impacted mainly by bulk changes to the over-all volume. Thus, we approximate (37) by keeping $\mathbf{I}_\mathrm{d}$ independent of $\boldsymbol{\Theta}$ for a single iteration of the gradient computation, that is,

$$\partial_g \mathbf{I}_\mathrm{d} \approx 0. \tag{39}$$

This bypasses the complexity of recursively computing $\partial_g \mathbf{I}_\mathrm{d}$.

It is important to note that at every iteration, the Jacobian $\nabla_\Theta \mathbf{I}[k]$ still **is** impacted by $\mathbf{I}_\mathrm{d}$. This is because $\mathbf{I}_\mathrm{d}$ affects $\mathbf{I}$ through Equation (12), and $\mathbf{I}$ appears in the terms $A_1, \ldots, A_6$. As the estimated medium properties evolve through iterations, so does $\mathbf{I}_\mathrm{d}$ (in `Step 1`, above). We just assume during `Step 2` that $\partial_g \mathbf{I}_\mathrm{d}$ is negligible compared to other terms in Equation (35).

Contrary to $\mathbf{I}_\mathrm{d}$, the single-scattered component is highly sensitive to changes in the micro-physical properties of a single voxel. We therefore include an exact treatment of single-scattering in the gradient computation (Appendix B). This is the essence of our numerical optimization approach. It enables tackling multiple-scattering tomography, in practice. Simulation results presented in the following section rely on additional numerical considerations (e.g., initialization, preconditioning, convergence criteria), which are all described in the accompanying Appendix D.

4. Computational Efficiency

Sections 3.2 and 3.3 describe our iterative gradient-based approach to Equations (28) and (29). The approach relies on an approximate Jacobian. We argue that our gradient computation is efficient,

relative to the state of the art. Recall that the goal is estimation of three unknown cloud-droplet parameters per voxel. Each Jacobian component expresses differentiation relative to *each* parameter in *each* voxel. Accounting for the need to run the forward model in Equation (28) and the Jacobian, brute force computation requires $3N_{\text{grid}} + 1$ full 3D vRTE computations, for each iteration of the optimization.

An alternative tractable approach relies on *adjoint* differentiation of 3D vRTE. To the best of our knowledge, only Martin et al. [75] have at least formulated a potentially efficient atmosphere/surface tomography based on the *adjoint* 3D vector RTE. However, the method was only demonstrated using 2D *scalar* RT, showing promise in retrieving cloud extinction [76]. The adjoint approach requires computing one full 3D vRTE and one full adjoint-3D vRTE, per gradient computation. Due to symmetry, the overall complexity of each iteration of the optimization would be that of *two* 3D-vRTE computations.

Our method to approximate the gradient per iteration requires lower resources: *one* forward full 3D vRTE (for Equation (28)) computation and a simple *single-scattering* computation. Intuitively, our approach compromises gradient accuracy at voxels where the adjoint Stokes vector has undergone multiple scattering events. These voxels will tend to be at larger optical distances from the sensors. The scattering events cause a decorrelation of the adjoint Stokes vector from the optical properties and therefore loss of sensitivity to the properties of individual voxels. The measurement sensitivity to cloud properties is therefore expected to diminish. Thus, while the accuracy of the gradient in these voxels is reduced, so is the magnitude of the gradient. This region of diminished sensitivity coincides with the "hidden core" of the cloud. We refer the reader to Forster et al. [77] for more details on the hidden core concept.

5. Simulations

In the context of tomography, *simultaneity* is defined by the evolution timescales of targeted clouds and by the time it takes to acquire multi-angular data. Becasue updraft timescales of shallow cumulus are $\sim 15min$ [78], our target clouds significantly evolve over a typical single-platform observation time span (e.g., 7 min for Terra's MISR). Hence, single-platform systems do not satisfy simultaneity in out context. As mentioned, real data of simultaneous spaceborne multi-angular polarimetric images of clouds does not yet exist, but a mission to supply this data is in the works. Therefore, we use careful simulations to test the approach. We simulate an atmosphere with molecular Rayleigh scattering and liquid water clouds. Rayleigh scattering is calculated from the Air Force Geophysics Laboratory (AFGL) database [79] for a summer mid-latitude atmosphere. Mie tables are pre-computed for $r_{\text{e}} \in [4, 25]$ µm and $v_{\text{e}} = 0.1$ with $N_{r_{\text{e}}} = 100$. The surface is Lambertian with a water-like albedo of 0.05. For realistic complexity, a Large Eddy Simulation (LES) model [80] was used to generate a cloud field. Each voxel is of size $20 \times 20 \times 40$ m^3. The LES outputs [80] are clouds with 3D variable LWC and 1D (vertically) variable r_{e}. A typical value [81] of $v_{\text{e}} = 0.1$ was chosen. Consequently, the present recovery demonstrations recover LWC and r_{e} on their respective native LES grid. On the other hand, $v_{\text{e}} = 0.1$ is excluded from the unknowns. The assumption of fixed v_{e} is not fundamental to our approach or implementation, however, relaxing this assumption warrants an investigation which will be done in future work. The spatial variability of the recovered parameters is discussed in more detail in Section 6.

From the generated cloud field, two isolated cloudy regions are taken for reconstruction:

1. `Scene A`: An atmospheric domain of dimensions $0.64 \times 0.72 \times 20$ km^3 with an isolated cloud (see synthetic AirMSPI nadir view in Figure 8).
2. `Scene B`: An atmospheric domain of dimensions $2.42 \times 2.1 \times 8$ km^3 with several clouds of varying optical thickness (see synthetic AirMSPI nadir view in Figure 9).

Synthetic measurements rendered with the spatial resolution and angular sampling of AirMSPI [14], namely, 10 m pixels and 9 viewing angles: $\pm 70.5°$, $\pm 60°$, $\pm 45.6°$, $\pm 26.1°$, and $0°$ from zenith, where $\pm$ indicates fore- and aft-views along the northbound flight path. The solar zenith angle is $15°$ from nadir in the measurement plane, that is, $0°$ solar azimuth. We simulate measurements at AirMSPI's three

polarized spectral bands: $\lambda = [0.47, 0.66, 0.865]$ µm. The bandwidths are narrow enough (≈46 nm) to render images using a single representative wavelength per band.

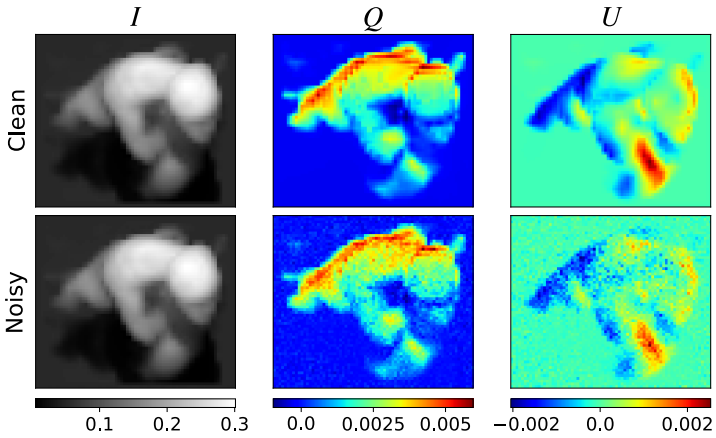

Figure 8. `Scene A` synthesized Stokes image using vSHDOM, before and after the application of a realistic AirMSPI noise model. We show here the *Bidirectional Reflectance Factor* (BRF) of the nadir view at $\lambda = 0.67$ µm.

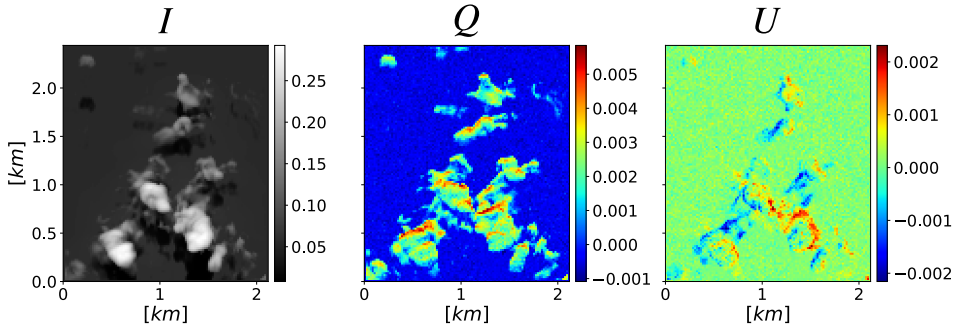

Figure 9. `Scene B` synthesized Stokes using vSHDOM. We show here the BRF of the nadir view at $\lambda = 0.67$ µm.

Single scattering albedos for these wavelengths equal unity (up to 4 significant digits). In other words, and in sharp contrast with the operational Nakajima–King [9] two-wavelengths non-tomographic retrieval, absorption by droplets plays no role in this demonstration of the tomography of cloud microphysics. The measurements are synthesized with realistic noise, according to the AirMSPI data acquisition model (see Appendix C).

Qualitative volumetric results of the recovered LWC for `Scene A` are shown in Figure 10. Scatter plot of the recovered LWC and the recovery results of r_e for `Scene A` are given in Figure 11. Qualitative volumetric results of the recovered LWC for `Scene B` are shown in Figure 12. A scatter plot of the recovered LWC and the recovery results of r_e for `Scene B` are given in Figure 13.

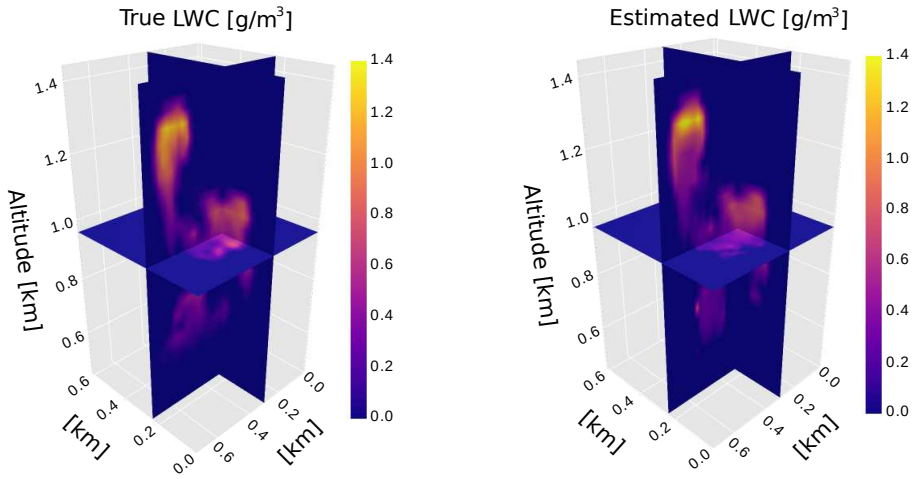

Figure 10. `Scene A` recovery results. (**Left**) Slices of the true cloud generated by Large Eddy Simulation (LES). (**Right**) Slices of the cloud estimated tomographically using AirMSPI polarized bands.

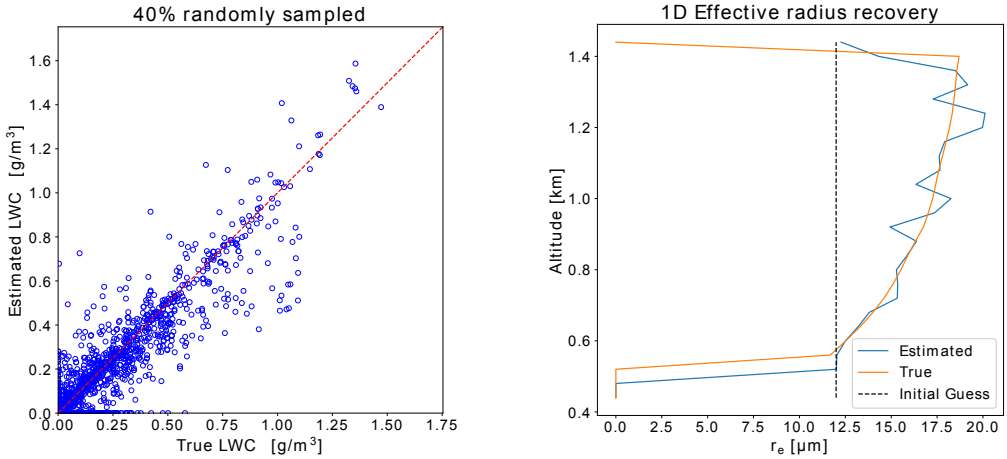

Figure 11. `Scene A` recovery results. (**Left**) Scatter plot of estimated vs. true Liquid Water Content (LWC). The correlation coefficient is 0.94, the Root Mean Square (RMS) is 0.065 g/m^3 and the bias is -0.002 g/m^3. (**Right**) recovery results of the 1D effective radius.

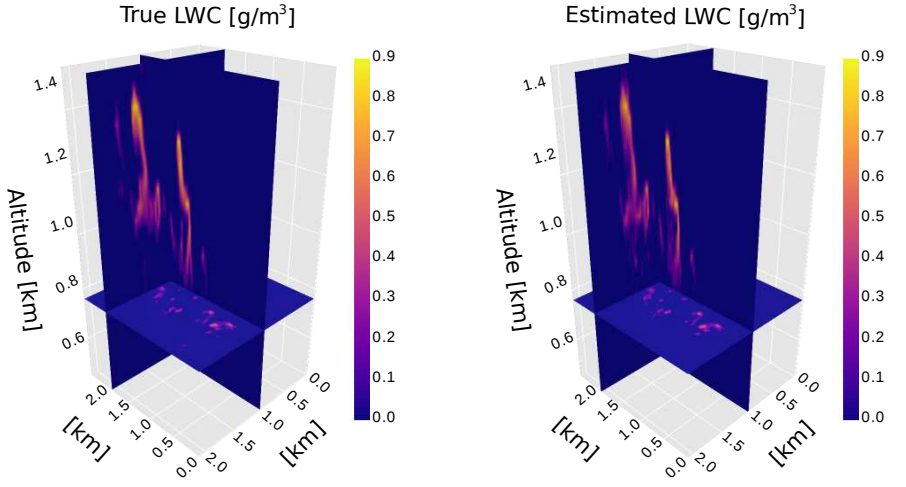

Figure 12. `Scene B` recovery results. (**Left**) Slices of the true LES generated region. (**Right**) Slices of the estimated region.

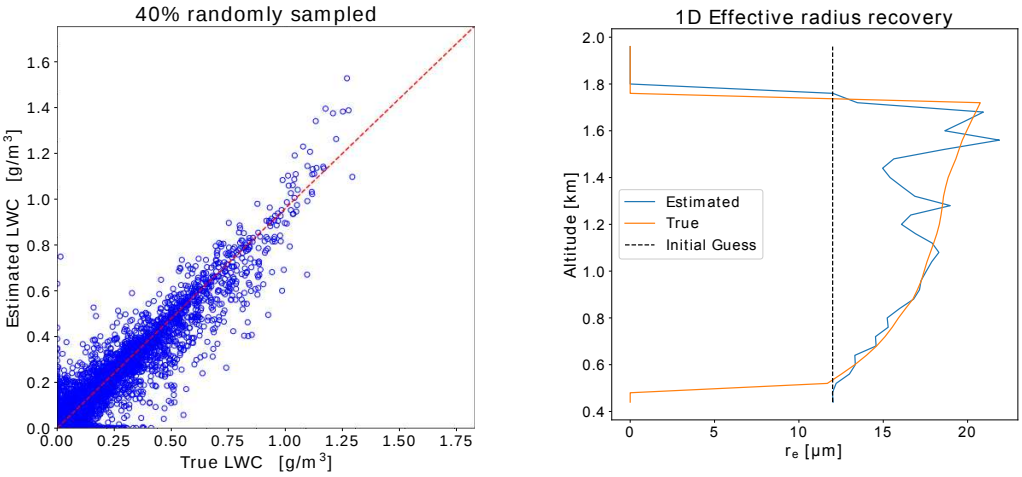

Figure 13. `Scene B` (**Left**) Scatter plot of the estimated vs. true LWC. The fit correlation is 0.96, the RMS is 0.085 g/m^3 and the bias is -0.0035 g/m^3. (**Right**) Recovery results of the 1D effective radius.

For quantitative assessment of the recovery, we use local mean error ϵ, and global bias measures [53] ϑ:

$$\epsilon_{\mathrm{LWC}} = \frac{\|\hat{\mathrm{LWC}}-\mathrm{LWC}\|_1}{\|\mathrm{LWC}\|_1}, \quad \vartheta_{\mathrm{LWC}} = \frac{\|\hat{\mathrm{LWC}}\|_1-\|\mathrm{LWC}\|_1}{\|\mathrm{LWC}\|_1}, \quad \epsilon_{r_e} = \frac{\|\hat{r_e}-r_e\|_1}{\|r_e\|_1}. \tag{40}$$

We further define the Root Mean Square (RMS) error and bias of the retrieved LWC as:

$$\mathrm{RMS} = \frac{1}{\sqrt{N_{\mathrm{grid}}}}\|\hat{\mathrm{LWC}}-\mathrm{LWC}\|_2^1, \quad \mathrm{bias} = \frac{1}{N_{\mathrm{grid}}}\sum_{g=1}^{N_{\mathrm{grid}}}(\hat{\mathrm{LWC}}[g]-\bar{\mathrm{LWC}}[g]). \tag{41}$$

The quantitative error measures upon convergence for the two scenes are:
`Scene A`: $\epsilon_{r_e}\approx$11%, $\epsilon_{\mathrm{LWC}}\approx$30%, $\vartheta_{\mathrm{LWC}}\approx -4$%, RMS$\approx$0.065 g/m^3, bias≈ -0.002 g/m^3,
`Scene B`: $\epsilon_{r_e}\approx$13%, $\epsilon_{\mathrm{LWC}}\approx$29%, $\vartheta_{\mathrm{LWC}}\approx -5$%, RMS$\approx$0.085 g/m^3, bias≈ -0.0035 g/m^3.
Using a 2.50 GHz CPU, the recovery run-time of cloud properties in `Scenes A,B` was $\sim$13 hours and $\sim$10 days, respectively.

Multi-angular tomographic retrieval enables vertical resolution of the droplet effective radius. By contrast, a homogeneous droplet radius is typically retrieved by mono-angular observations fitted to a plane-parallel homogeneous cloud model. The retrieval errors of droplet radii in the demonstrations above are significantly smaller than retrieval errors of a homogeneous droplet radius. The latter can easily exceed 50% in similar conditions to our study that is, shallow cumuli and illumination conditions (see e.g., Reference [82]).

6. Discussion

In the formulation of our retrieval, and in nature, the droplet effective radius r_e and droplet effective variance v_e vary in 3D. This allows us to, in principle, localize the variations in cloud microphysical properties which is a significant advance over other methods. Operational remote sensing algorithms, which rely on 1D RT and plane-parallel cloud models, retrieve a single value for r_e (and for v_e), for each cloudy pixel. This occurs both in bi-spectral [9,83] and polarimetric [11,84] techniques. The physical interpretation is complicated by the difficulty in determining which portion of the cloud the retrieved quantities corresponds to.

In our current demonstrations we assume 1D variable r_e and a completely homogeneous v_e. This is much more general than operational methods, but still a degenerate representation compared to full 3D variability. We now discuss the realism of such a representation.

Vertically varying droplet size distributions arise as a result of moist adiabatic thermodynamics in vertically stratified environments (e.g., Reference [81]). Further 3D variability forms due to the diabatic mixing of air parcels in the turbulent processes of entrainment and detrainment. Despite the complexity of these processes, there is evidence that the horizontal variability r_e is indeed small over a cloud scale.

This evidence comes from in-situ aircraft observations of shallow cumulus [85–87], modelling studies [88] and theory [89]. However, there are also select observations of monsoonal clouds [90] and theoretical arguments [89] that suggest there is a sharp gradient in the droplet effective radius in the very outer shell of the clouds. If this is the case, then a representation having vertical-only variation of r_e loses validity at the outer shell.

The value of v_e can also vary significantly across different environmental conditions. This is seen in research flights including in-situ measurements [91–95]. Moreover, in LES simulations of shallow cumulus clouds with bin microphysics, v_e might range from 0.01 to 0.26 [96]. The core of a cloud tends to have a low effective variance as condensation is the dominant process there [96,97]. Cloud edges, in contrast, experience also evaporation and entrainment mixing, as the cloud is diluted by environmental air [98]. This tends to increase v_e. If the cloud has precipitation, spatial variability of v_e increases [99].

While horizontal variations reduce the accuracy of our demonstrated retrieval, these points show that the approximations used in our demonstrations are often reasonable and a significant advance. To further push the potential of the general framework proposed here and retrieve additional degrees of freedom describing microphysical variations in 3D, we may include more information. One option is to include additional measurements, for example, by using a combination of AirMSPI [14] and Research Spectro-Polarimeter (RSP) [100]. Another option is to introduce regularization schemes, which mathematically express the natural trends of horizontal variability mentioned above. The 3D tomographic approach presented in the paper offers a lot more flexibility than current operational analyses and enables the development and application of retrievals that might provide new insight into cloud microphysics.

7. Summary & Outlook

We derive the tomography of cloud microphysics based on multi-view/multi-spectral polarimetric measurements of scattered sunlight. This novel type of tomography uses, for the first time, 3D polarized RT as the image formation model. The recovery of droplet sizes is made possible due to the crucial phase-function information carried by the polarized signal. We define a model-fitting error function and compute approximate gradients of this function to make the recovery tractable. Demonstration are done on synthetic 3D clouds, based on a Large Eddy Simulation with the effective radius assumed to vary only vertically. Our open-source code is publicly available [101].

Future work will address the extent to which polarimetric measurements penetrate the cloud and the relation between r_e in the *outer shell* and r_e in the cloud *core*, as defined by Forster et al. [77]. Furthermore, we will relax the fixed v_e assumption that was used in the demonstrations, and thus assess full microphysical retrieval capabilities of polarization measurements. Moreover, future plans include experimental demonstration and use, while the CloudCT formation orbits. Research is ongoing [77] about the adaptation of our cloud tomography methodology for satellite data as can be obtained from the multi-view imaging from MISR on Terra and a SWIR view from the collocated MODIS, but with significantly lower spatial resolution than used so far.

Lastly, we note that our atmospheric tomography approach described herein can be adapted to aerosols, including dense plumes of wild fire smoke, volcanic ash, and dust near their sources. The main difference in this extended application is that the forward model must be further linearized with respect to the complex refractive index of the varying aerosol material, which has been done for 1D polarized RT (e.g., Reference [102]), even for non-sphericity effects (e.g., Reference [103]).

Author Contributions: Conceptualization, A.L. and Y.Y.S.; methodology, A.L., Y.Y.S., A.B.D.; software, A.L., J.L.; validation, A.L. and J.L.; formal analysis, A.L.; investigation, A.L.; resources, Y.Y.S.; data curation, A.L. and J.L.;

writing—original draft preparation, A.L.; writing—review and editing, A.L., Y.Y.S., A.B.D. and J.L.; visualization, A.L.; supervision, Y.Y.S.; project administration, A.L. and Y.Y.S.; funding acquisition, Y.Y.S. All authors have read and agreed to the published version of the manuscript.

Funding: The authors are grateful to the US-Israel Binational Science Foundation (BSF grant 2016325) for continuously facilitating our international collaboration. Aviad Levis' work was partially supported as a Zuckerman Foundation STEM Leadership Fellow. Yoav Schechner is a Landau Fellow supported by the Taub Foundation. His work was conducted in the Ollendorff Minerva Center (BMBF). Anthony Davis' work was carried out at JPL/Caltech, supported by NASA's SMD/ESD/(RST+TASNPP) and ESTO/AIST programs. That research was carried out at the Jet Propulsion Laboratory, California Institute of Technology, under a contract with the National Aeronautics and Space Administration (80NM0018D0004). Support for Jesse Loveridge's work from JPL under contract #147871 is gratefully acknowledged. This project has received funding from the European Research Council (ERC) under the European Union's Horizon 2020 research and innovation program (grant agreement No 810370: CloudCT).

Acknowledgments: We thank I. Koren, D. Rosenfeld, A. Aides, D. Diner, L. Di Girolamo, and G. Matheou for support and fruitful discussions. We acknowledge F. Evans and A. Doicu for the online vSHDOM code.

Conflicts of Interest: The authors declare no conflict of interest.

Appendix A. Extended Theoretical Background

Appendix A.1. Scatterer Microphysical Properties

In the lower atmosphere, cloud particles are droplets of liquid water that are very nearly spherical, having radius r. They are however polydisperse, with a droplet size distribution denoted $n(r)$. For most remote-sensing purposes, $n(r)$ is parameterized using an *effective radius* in μm and a dimensionless *variance* [66]:

$$r_{\mathrm{e}} = \frac{\int_0^\infty r^3 n(r)\mathrm{d}r}{\int_0^\infty r^2 n(r)\mathrm{d}r}, \quad v_{\mathrm{e}} = \frac{\int_0^\infty (r-r_{\mathrm{e}})^2 r^2 n(r)\mathrm{d}r}{r_{\mathrm{e}}^2 \int_0^\infty r^2 n(r)\mathrm{d}r}. \tag{A1}$$

A commonly used parametric size distribution with empirical support [66] is the *Gamma*-distribution (Figure 2):

$$n(r) = N\, c\, r^{(v_{\mathrm{e}}^{-1}-3)} \exp[-r/(r_{\mathrm{e}} v_{\mathrm{e}})], \tag{A2}$$

where we require $0 < v_{\mathrm{e}} < 1/2$. Here $c = (r_{\mathrm{e}} v_{\mathrm{e}})^{(2-v_{\mathrm{e}}^{-1})}/\Gamma(v_{\mathrm{e}}^{-1}-2)$ is a normalization constant and

$$N = \int_0^\infty n(r)\mathrm{d}r \tag{A3}$$

is the droplet number concentration. Let ρ_{w} be the density of liquid water. An important cloud characteristic is the water mass density or *Liquid Water Content* (LWC) per unit volume:

$$\mathrm{LWC} = \frac{4}{3}\pi\rho_{\mathrm{w}} \int_0^\infty r^3 n(r)\mathrm{d}r. \tag{A4}$$

It is expressed as $\mathrm{LWC} = {}^4/_3\, \pi\rho_{\mathrm{w}} r_{\mathrm{e}}^3 (1-v_{\mathrm{e}})(1-2v_{\mathrm{e}})$ for the Gamma distribution in (A2). In Section 3 these microphysical parameters, LWC, $r_{\mathrm{e}}, v_{\mathrm{e}}$, are unknown quantities we seek to estimate on a 3D grid.

Appendix A.2. Polarized Light

A light wave is associated with orthogonal components of a random electric wave, $E_1(t)$ and $E_2(t)$, where t is time. The components' direction unit vectors are respectively $\hat{\mathbf{E}}_1$ and $\hat{\mathbf{E}}_2$. The wave propagates in direction $\boldsymbol{\omega} = \hat{\mathbf{E}}_1 \times \hat{\mathbf{E}}_2$. It is convenient to define the polarized light state in terms of the Stokes [66] vector $\mathbf{I} = (I, Q, U, V)^\top$. Each component of $\mathbf{I}$ expresses temporal integration:

$$\begin{aligned} I &= \langle E_1 E_1^* + E_2 E_2^* \rangle_t, \quad Q = \langle E_1 E_1^* - E_2 E_2^* \rangle_t, \\ U &= \langle E_1 E_2^* + E_2 E_1^* \rangle_t, \quad V = \mathrm{i}\langle E_1 E_2^* - E_2 E_1^* \rangle_t, \end{aligned} \tag{A5}$$

where $\mathrm{i} = \sqrt{-1}$. Unpolarized intensity is I. The degrees of polarization (DOP) and linear polarization (DoLP) are respectively defined as the ratios $\sqrt{Q^2+U^2+V^2}/I$, $\sqrt{Q^2+U^2}/I$. The angle of linear polarization (AoLP) is $1/2\ \tan^{-1}(U/Q)$.

Appendix A.3. Single Scattering of Polarized Light

Light interaction with a single particle is described by the total extinction cross-section $s_\mathrm{t}(r,\lambda)$, decomposed into scattering and absorption cross-sections, respectively:

$$s_\mathrm{t}(r,\lambda) = s_\mathrm{s}(r,\lambda) + s_\mathrm{a}(r,\lambda). \tag{A6}$$

In Mie scattering by spheres, introduced further on, we have

$$s_\mathrm{t}(r,\lambda) = \pi r^2\, \mathcal{Q}_\mathrm{t}(2\pi r/\lambda), \quad s_\mathrm{s}(r,\lambda) = \pi r^2\, \mathcal{Q}\mathrm{s}(2\pi r/\lambda), \quad s_\mathrm{a}(r,\lambda) = \pi r^2\, \mathcal{Q}\mathrm{a}(2\pi r/\lambda), \tag{A7}$$

where $\mathcal{Q}$t, $\mathcal{Q}$s, $\mathcal{Q}$a are dimensionless efficiency factors, which depend on the normalized size parameter $2\pi r/\lambda$. In the limit $r \gg \lambda$, $\mathcal{Q}\mathrm{t} \approx 2$. Furthermore, when $s_\mathrm{s}(r,\lambda) \gg s_\mathrm{a}(r,\lambda)$, then $\mathcal{Q}\mathrm{s} \approx 2$ and $\mathcal{Q}\mathrm{a} \approx 0$.

When molecular absorption can be neglected, material optical properties can be approximated using a single wavelength for each narrow spectral band. This approximation, commonly used in multi-spectral remote sensing, relies on a single rendering of spectrally-averaged optical properties. It is valid if wavelength dependencies within a spectral band are weak, a condition met when narrow bands are considered. Macroscopic optical cross-sections are then expressed as weighted averages

$$\sigma_\mathrm{t}(\lambda) = \langle s_\mathrm{t}(r,\lambda)\rangle_r,\ \sigma_\mathrm{s}(\lambda) = \langle s_\mathrm{s}(r,\lambda)\rangle_r,\ \sigma_\mathrm{a}(\lambda) = \langle s_\mathrm{a}(r,\lambda)\rangle_r. \tag{A8}$$

We note that (A8) aggregates scattering properties rather than electric fields. This aggregation holds for scatterer populations that are in each other's far field (i.e., are $\gg \lambda$ apart) [66]. Here the size-weighted average over some function $a(r)$ is defined by

$$\langle a\rangle_r = \frac{1}{N}\int_0^\infty a(r)n(r)\mathrm{d}r. \tag{A9}$$

The size integral of (A9) is terminated in practice at r_max = 70 µm. Note that throughout the text, dependency on λ is generally omitted for simplicity; however, it is used at specific points as needed.

Scattering, as a fraction of the overall interaction [67], is expressed by the dimensionless *single scattering albedo*

$$\varpi = \frac{\sigma_\mathrm{s}}{\sigma_\mathrm{t}}. \tag{A10}$$

The extinction coefficient (or optical density) is denoted by β. Following Equations (A3), (A4) and (A8), $\beta = N\sigma_\mathrm{t}$ is expressed in terms of the LWC as [68]

$$\beta = \frac{\mathrm{LWC}}{\frac{4}{3}\pi\rho_w\langle r^3\rangle_r}\sigma_\mathrm{t} = \mathrm{LWC}\cdot\tilde{\sigma}_\mathrm{t}. \tag{A11}$$

Here, $\tilde{\sigma}_\mathrm{t}$ is the mass extinction coefficient (in units of m^2/g).

Let $\boldsymbol{\omega}$ and $\boldsymbol{\omega}'$ be the unitary incident and scattered ray direction vectors respectively in Figure 2. Single-scattering geometry is defined by the local coordinate system of the incoming beam's electric fields. As stated above, the electric field of incoming light is decomposed into components along orthogonal directions. We set them as

$$\mathbf{E}_1 \propto \boldsymbol{\omega}\times\boldsymbol{\omega}', \quad \mathbf{E}_2 \propto \mathbf{E}_1\times\boldsymbol{\omega}. \tag{A12}$$

The scattering angle is $\theta = \cos^{-1}(\boldsymbol{\omega}\cdot\boldsymbol{\omega}')$. The angular redistribution of singly-scattering light from a sphere of is defined by the 4×4 dimensionless *Mueller* matrix $\mathbf{P}_{\mathrm{s}}(\theta, r)$. The macroscopic *phase matrix* is the size-weighted average

$$\mathbf{P}(\theta) = \frac{\langle s_{\mathrm{s}}(r)\mathbf{P}_{\mathrm{s}}(\theta, r)\rangle_r}{\sigma_{\mathrm{s}}}. \tag{A13}$$

For spherical (or just randomly-oriented) particles, the phase-matrix $\mathbf{P}(\theta)$ takes the following symmetric form [66]

$$\mathbf{P}(\theta) = \begin{bmatrix} p_{11}(\theta) & p_{21}(\theta) & 0 & 0 \\ p_{21}(\theta) & p_{22}(\theta) & 0 & 0 \\ 0 & 0 & p_{33}(\theta) & -p_{43}(\theta) \\ 0 & 0 & p_{43}(\theta) & p_{44}(\theta) \end{bmatrix}, \tag{A14}$$

where p_{11} is the (unpolarized) scattering phase-function. In single-scattering of unpolarized incident sunlight, the DoLP of scattered light amounts to the ratio $|p_{21}|/p_{11}$.

Appendix A.3.1. Rayleigh Scattering

The Rayleigh model describes light scattering by particles much smaller than the wavelength. The Rayleigh phase matrix takes the following form [70]

$$\mathbf{P}_{\mathrm{Rayl}}(\theta) = \begin{bmatrix} \frac{3}{4}(1+\cos^2\theta) & -\frac{3}{4}\sin^2\theta & 0 & 0 \\ -\frac{3}{4}\sin^2\theta & \frac{3}{4}(1+\cos^2\theta) & 0 & 0 \\ 0 & 0 & \frac{3}{2}\cos\theta & 0 \\ 0 & 0 & 0 & \frac{3}{2}\cos\theta \end{bmatrix}. \tag{A15}$$

The single-scattering DoLP due to air molecules is then

$$\mathrm{DoLP}_{\mathrm{Rayl}}(\theta) = \frac{\sin^2\theta}{1+\cos^2\theta}. \tag{A16}$$

According to (A16) a maximum DoLP is attained at single-scattering angle $\theta = 90°$.

Appendix A.3.2. Mie Scattering

Mie theory describes how light interacts with a spherical particle of size comparable to λ [69]. Denote $\mu = \cos\theta$. Mie scattering is defined in terms of complex-valued amplitude scattering functions $S_1(\mu), S_2(\mu)$, which correspond to scattering of the E_1, E_2 electric field components. Scattering of the Stokes vector $\mathbf{I}$ is described by the phase matrix $\mathbf{P}_{\mathrm{Mie}}(\mu)$, which is fully defined by six matrix components:

$$\begin{aligned} p_{11}^{\mathrm{Mie}} &= \frac{\varrho}{2}(S_1S_1^* + S_2S_2^*), \quad p_{12}^{\mathrm{Mie}} = \frac{\varrho}{2}(S_1S_1^* - S_2S_2^*), \\ p_{22}^{\mathrm{Mie}} &= \frac{\varrho}{2}(S_1S_1^* + S_2S_2^*), \quad p_{33}^{\mathrm{Mie}} = \frac{\varrho}{2}(S_1S_2^* + S_2S_1^*), \\ p_{43}^{\mathrm{Mie}} &= \frac{\varrho}{2}(S_1S_2^* - S_2S_1^*), \quad p_{44}^{\mathrm{Mie}} = \frac{\varrho}{2}(S_1S_2^* + S_2S_1^*). \end{aligned} \tag{A17}$$

Here, ϱ is a normalization constant, set to satisfy $\frac{1}{2}\int_{-1}^{1} p_{11}^{\mathrm{Mie}}(\mu)\mathrm{d}\mu = 1$.

Mie scattering due to water droplets peaks at specific angles. For a single droplet or monodisperse material, $\mathbf{P}^{\mathrm{Mie}}$ has sharp scattering lobes at angles that depend on the droplet's r/λ ratio. A macroscopic voxel contains droplets in a range of radii r, smoothing the scattering lobes. The smoothing effect depends on v_{e} (Figure 3). Two angular domains that stand out for remote-sensing purposes are the cloud-bow ($\theta \in [135°, 155°]$) and glory ($\theta \in [175°, 180°]$). Both domains have peaks that are sensitive to

the droplet microphysical parameters, and are significantly polarized (i.e., peaks are visible in the p_{12}^{Mie} component). The latter fact renders these peaks distinguishable in the presence of a multiply-scattered signal component.

Appendix B. Jacobian Derivation

In Equation (35) of the main text, the Jacobian is written as a sum of six terms

$$\partial_g \mathbf{I}[k] = A_1 + A_2 + A_3 + A_4 + A_5 + A_6. \tag{A18}$$

In this section we expand and describe each of these terms. Using Equations (7) and (19), the transmittance derivative is

$$\partial_g T\left(\boldsymbol{x}_1 \to \boldsymbol{x}_2\right) = -T\left(\boldsymbol{x}_1 \to \boldsymbol{x}_2\right) \ell_g\left(\boldsymbol{x}_1 \to \boldsymbol{x}_2\right) \partial_g \beta. \tag{A19}$$

Then,

$$A_1 = -\ell_g\left(\boldsymbol{x}_0 \to \boldsymbol{x}_k\right) \mathbf{I}\left(\boldsymbol{x}_0, \boldsymbol{\omega}_k\right) T\left(\boldsymbol{x}_0 \to \boldsymbol{x}_k\right) \left[\partial_g \beta\right], \tag{A20}$$

$$A_2 = \ell_g\left(\boldsymbol{x}_0 \to \boldsymbol{x}_k\right) \int_{\boldsymbol{x}_0}^{\boldsymbol{x}_k} \left[\frac{\partial_g \varpi}{4\pi} \int_{4\pi} \mathbf{P}\left(\boldsymbol{x}', \boldsymbol{\omega}_k \cdot \boldsymbol{\omega}'\right) \mathbf{I}\left(\boldsymbol{x}', \boldsymbol{\omega}'\right) \mathrm{d}\boldsymbol{\omega}'\right] \beta(\boldsymbol{x}') T\left(\boldsymbol{x}' \to \boldsymbol{x}_k\right) \mathrm{d}\boldsymbol{x}', \tag{A21}$$

$$A_3 = \ell_g\left(\boldsymbol{x}_0 \to \boldsymbol{x}_k\right) \int_{\boldsymbol{x}_0}^{\boldsymbol{x}_k} \left\{\frac{\varpi(\boldsymbol{x}')}{4\pi} \int_{4\pi} \left[\partial_g \mathbf{P}\left(\boldsymbol{x}', \boldsymbol{\omega}_k \cdot \boldsymbol{\omega}'\right)\right] \mathbf{I}\left(\boldsymbol{x}', \boldsymbol{\omega}'\right) \mathrm{d}\boldsymbol{\omega}'\right\} \beta(\boldsymbol{x}') T\left(\boldsymbol{x}' \to \boldsymbol{x}_k\right) \mathrm{d}\boldsymbol{x}', \tag{A22}$$

$$A_4 = \int_{\boldsymbol{x}_0}^{\boldsymbol{x}_k} \left\{\frac{\varpi(\boldsymbol{x}')}{4\pi} \int_{4\pi} \mathbf{P}\left(\boldsymbol{x}', \boldsymbol{\omega}_k \cdot \boldsymbol{\omega}'\right) \left[\partial_g \mathbf{I}\left(\boldsymbol{x}', \boldsymbol{\omega}'\right)\right] \mathrm{d}\boldsymbol{\omega}'\right\} \beta(\boldsymbol{x}') T\left(\boldsymbol{x}' \to \boldsymbol{x}_k\right) \mathrm{d}\boldsymbol{x}', \tag{A23}$$

$$A_5 = \ell_g\left(\boldsymbol{x}_0 \to \boldsymbol{x}_k\right) \left[\partial_g \beta\right] \int_{\boldsymbol{x}_0}^{\boldsymbol{x}_k} \mathbf{J}\left(\boldsymbol{x}', \boldsymbol{\omega}_k\right) T\left(\boldsymbol{x}' \to \boldsymbol{x}_k\right) \mathrm{d}\boldsymbol{x}', \tag{A24}$$

$$A_6 = -\ell_g\left(\boldsymbol{x}_0 \to \boldsymbol{x}_k\right) \left[\partial_g \beta\right] \int_{\boldsymbol{x}_0}^{\boldsymbol{x}_k} \mathbf{J}\left(\boldsymbol{x}', \boldsymbol{\omega}_k\right) \beta(\boldsymbol{x}') T\left(\boldsymbol{x}' \to \boldsymbol{x}_k\right) \mathrm{d}\boldsymbol{x}'. \tag{A25}$$

Note that $\mathbf{I}\left(\boldsymbol{x}, \boldsymbol{\omega}\right)$ and $\mathbf{J}\left(\boldsymbol{x}, \boldsymbol{\omega}\right)$ are computed in `Step 1` and are therefor ready for use when computing A_1, A_2, A_3, A_5 and A_6. Furthermore, $\ell_g\left(\boldsymbol{x}_0 \to \boldsymbol{x}_k\right) = 0$ for any voxel that is not on the LOS of pixel k. Therefore, the terms A_1, A_2, A_3, A_5, A_6 are computed using a single path tracing $\boldsymbol{x}_k \to \boldsymbol{x}_0$.

We now give special attention to A_4 in Equation (A23). Using the diffuse-direct decomposition of (12), we decompose (A23) as

$$\begin{aligned} A_4 = & \int_{\boldsymbol{x}_0}^{\boldsymbol{x}_k} \left\{\frac{\varpi(\boldsymbol{x}')}{4\pi} \int_{4\pi} \mathbf{P}\left(\boldsymbol{x}', \boldsymbol{\omega}_k \cdot \boldsymbol{\omega}'\right) \left[\partial_g \mathbf{I}_{\mathrm{d}}\left(\boldsymbol{x}', \boldsymbol{\omega}'\right)\right] \mathrm{d}\boldsymbol{\omega}'\right\} \beta(\boldsymbol{x}') T\left(\boldsymbol{x}' \to \boldsymbol{x}_k\right) \mathrm{d}\boldsymbol{x}' \\ & + \int_{\boldsymbol{x}_0}^{\boldsymbol{x}_k} \left\{\frac{\varpi(\boldsymbol{x}')}{4\pi} \int_{4\pi} \mathbf{P}\left(\boldsymbol{x}', \boldsymbol{\omega}_k \cdot \boldsymbol{\omega}'\right) \delta\left(\boldsymbol{\omega}' - \boldsymbol{\omega}_{\mathrm{Sun}}\right) \mathbf{F}_{\mathrm{Sun}} \left[\partial_g T\left(\boldsymbol{x}_{\mathrm{Sun}} \to \boldsymbol{x}'\right)\right] \mathrm{d}\boldsymbol{\omega}'\right\} \beta(\boldsymbol{x}') T\left(\boldsymbol{x}' \to \boldsymbol{x}_k\right) \mathrm{d}\boldsymbol{x}'. \end{aligned} \tag{A26}$$

The first term in (A26) is based on $\partial_g \mathbf{I}_{\mathrm{d}}$, i.e., a derivative of the diffuse (high order scattering) component. Herein lies a recursive complexity. In principle, a differential change in the microphysics of one voxel can recursively affect the radiance at every other voxel, and this affects all the pixels. To make calculations numerically efficient, we approximate (A26). The approximation assumes that relative to other components in the Jacobian, $\mathbf{I}_{\mathrm{d}}$ is less sensitive to a differential changes in the microphysical

properties at voxel g. Thus, (A26) is approximated by keeping $\mathbf{I}_{\mathrm{d}}$ independent of $\boldsymbol{\Theta}$ for a single iteration of the gradient computation, that is,

$$\partial_g \mathbf{I}_{\mathrm{d}} \approx 0 \,. \tag{A27}$$

The second term in (A26) is based on differentiation of the direct component. This is straight-forward to compute using (A19). Consequently, using Equation (A27) and the definition of $\mathbf{I}_{\mathrm{Single}}\left(\boldsymbol{x}_{\mathrm{Sun}} \rightarrow \boldsymbol{x}' \rightarrow \boldsymbol{x}_k\right)$ in (16), the term A_4 in (A26) is approximated by

$$A_4 \approx \tilde{A}_4 = \left[\partial_g \beta\right] \int_{\boldsymbol{x}_0}^{\boldsymbol{x}_k} \ell_g\left(\boldsymbol{x}_{\mathrm{Sun}} \rightarrow \boldsymbol{x}'\right) \mathbf{I}_{\mathrm{Single}}\left(\boldsymbol{x}_{\mathrm{Sun}} \rightarrow \boldsymbol{x}' \rightarrow \boldsymbol{x}_k\right) \mathrm{d}\boldsymbol{x}'. \tag{A28}$$

The term $\ell_g\left(\boldsymbol{x}_{\mathrm{Sun}} \rightarrow \boldsymbol{x}'\right)$ in (A28) contributes to voxels *outside* of the LOS. The integral in $\tilde{A}_4$ is computed with a *broken-ray* [104] path $\boldsymbol{x}_k \rightarrow \boldsymbol{x}' \rightarrow \boldsymbol{x}_{\mathrm{Sun}}$, as illustrated in Figure 4.

Using Equations (8), (A19), (A20) and (A25), A_1 and A_6 are combined to

$$A_{1,6} = A_1 + A_6 = -\left[\partial_g \beta\right] \mathbf{I}\left(\boldsymbol{x}_g, \boldsymbol{\omega}_k\right). \tag{A29}$$

Overall, in our iterative procedure, we approximate the Jacobian in (35) by

$$\partial_g \mathbf{I}[k] = A_{1,6} + A_2 + A_3 + \tilde{A}_4 + A_5. \tag{A30}$$

Equations (A20)–(A28) formulate the Jacobian in terms of a voxel grid (zero-order interpolation). However, in practice we use a trilinear interpolation kernel K in (18), consistent with vSHDOM internal interpolation [59].

Appendix C. Measurement Noise

The inverse problem defined in the main text is formulated in terms of measured Stokes vectors (Equation 21). However, Stokes vectors are not measured directly. Rather, they are derived from intensity measurements taken through filters. The raw intensity measurements are noisy. Noise is dominated by Poisson photon noise, which is independent across different raw measurements. However, the estimation of Stokes components *from* independent intensity measurements yields noise which is correlated across the components of the Stokes vector, per-pixel. In this section, we describe the synthesis model we employ to generate realistic noise in simulations. Our synthesis is based on the AirMSPI [105] sensor model. Furthermore, we derive the expression for $\mathbf{R}$, which we use in the recovery process (Equation (27) in the main text).

AirMSPI measures a modulated intensity signal at N_{sub}=23 subframes. Define a normalized frame which spans the unitless integration time interval $\psi \in [-0.5, 0.5]$. Denote the temporal center and span of each subframe as ψ_l and $\Delta\psi = 1/N_{\mathrm{sub}}$, respectively (Figure A1). Based on the sensing process described in Ref. [105], define the following modulation function, whose parameters are given in Table A1:

$$M[l] = J_0[\kappa(\psi_l)] + \frac{1}{3}\left(\frac{\pi\Delta\psi}{2}\right)^2 \gamma_0^2(\lambda)\Big\{J_2[\kappa(\psi_l)] - \cos[2(\pi\psi_l - \eta)]J_0[\kappa(\psi_l)]\Big\}, \tag{A31}$$

with

$$\kappa(\psi_l) = -2\gamma_0(\lambda)\sin(\pi\psi_l - \eta)\sqrt{1 + \cot^2(\pi\psi_l - \eta)}. \tag{A32}$$

Table A1. Modulation parameters [105] used for synthesis of AirMSPI measurements.

γ_0(470 nm)	γ_0(660 nm)	γ_0(865 nm)	ξ(470 nm)	ξ(660 nm)	ξ(865 nm)	η
4.472	3.081	2.284	1.0	0.27	0.03	0.009

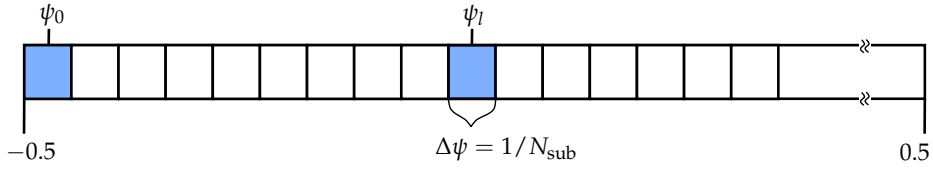

Figure A1. A normalized frame spans the interval $[-0.5, 0.5]$, evenly divided into N_{sub} subframes.

Here J_0, J_2 are the Bessel functions of the first kind of order 0 and 2, respectively. Denote by $\xi(\lambda)$ a wavelength-dependent ratio, which is drawn from quantum efficiencies and spectral bandwidths of each AirMSPI band (Table A1). For the exact calculation of the ratio see Equation (24) of [105]. Using simulated Stokes vectors derived by vSHDOM, AirMSPI measurements are synthesised as passing through two polarization analyzing filters [105]. As defined in Equation (11) in the main text, $\mathbf{I}[k]$ is the Stokes vector in pixel k. Correspondingly the intensity is $I[k]$, while $Q[k], U[k]$ are the polarized components. Measurements l through the two filters of AirMSPI are modeled by

$$d_0[l,k] = \xi(\lambda)\big(I[k] + M[l]Q[k]\big) \tag{A33}$$

$$d_{45}[l,k] = \xi(\lambda)\big(I[k] + M[l]U[k]\big), \tag{A34}$$

where $M[l]$ and $\xi(\lambda)$ are given in Equation (A31) and Table A1, respectively. The units of d are Watts. Define $\mathbf{d}[k] = \left(d_0[1,k], ..., d_0[N_{\text{sub}},k], d_{45}[1,k], ..., d_{45}[N_{\text{sub}},k]\right)^\top$. In matrix from, the transformations by Equations (A33) and (A34) are written using a single 46×3 modulation matrix $\mathbf{M}$

$$\mathbf{d}[k] = \mathbf{M}\mathbf{I}[k]. \tag{A35}$$

Detection is by a camera which generates photo-electrons in each pixel well. The relation between $d_0[l,k]$ or $d_{45}[l,k]$ and the *expected* unit-less number of photo-electrons in the pixel is given by a gain G. The number of photo-electrons is random (*Poissonian*) around this expected value. The vector of simulated electron counts is thus synthesized by a Poisson process

$$\mathbf{e}[k] \sim Poisson\Big\{\text{round}\left(G \cdot \mathbf{d}[k]\right)\Big\} = Poisson\Big\{\text{round}\left(G \cdot \mathbf{M}\mathbf{I}[k]\right)\Big\}. \tag{A36}$$

The gain G is chosen to let the maximum signal at each camera view (i.e. maximum over pixels, wavelengths and subframe measurements) reach the maximum *full-well depth* of 200,000 electrons, consistent with AirMSPI specifications. Equation (A36) synthesizes raw AirMSPI signals including noise (Figure 8). The synthesized AirMSPI signals, including this noise, are now used as inputs to the calculation of measured Stokes vectors in each pixel and viewpoint. The vector of electron counts $\mathbf{e}[k]$ in each pixel k is transformed into Stokes synthetic data (Equation (21)) using a 3×46 demodulation matrix $\mathbf{W}$

$$\mathbf{y}_\mathbf{I}[k] = (\mathbf{M}^\top\mathbf{M})^{-1}\mathbf{M}^\top\mathbf{e}[k] = \mathbf{W}\mathbf{e}[k]. \tag{A37}$$

The vectors $\mathbf{y}_\mathbf{I}[k]$ form the data for tomographic analysis.

Our tomographic analysis takes into account the noise properties, including noise correlation. As we now show, the measurement model (A37) yields correlated noise of different Stokes components. Thus, $\mathbf{R}^{-1}$ (in Equation (27)) is not diagonal. Denote the diagonal co-variance matrix of the photo-electron readings by $\mathbf{C}_\text{e}^{-1} = \text{diag}(\mathbf{e})$. Let $\mathcal{I}_{46\times46}$ denote the *Identity* matrix. The signal is generally dominated by unpolarized multiply-scattered background light. Relative to it, the magnitude of the

modulated polarization signal is small. Thus, per pixel k, the diagonal matrix $\mathbf{C}_{\mathrm{e}}^{-1}[k]$ is approximately constant with a global weight

$$\mathbf{C}_{\mathrm{e}}^{-1}[k] \approx \alpha[k]\mathcal{I}_{46\times 46}. \tag{A38}$$

Using Equations (A37) and (A38) for each pixel, the Stokes co-variance matrix is

$$\mathbf{C}^{-1}[k] = \mathbf{M}^{\top}\mathbf{C}_{\mathrm{e}}^{-1}[k]\mathbf{M} \approx \alpha[k]\mathbf{M}^{\top}\mathbf{M}. \tag{A39}$$

A maximum-likelihood estimator corresponding to a Poisson process should have a weight $\alpha[k] \propto 1/\|\mathbf{e}\|_1$, to account for higher photon noise in brighter pixels. In simulations, however, we found that $\alpha[k] = 1$ worked better. This is perhaps due to richer information carried by denser cloud regions, i.e. brighter pixels. Overall the expression we minimize in (27) is

$$\hat{\Theta} = \arg\min_{\Theta} \sum_{k=1}^{N_{\mathrm{meas}}} \left(\mathbf{I}[k] - \mathbf{y}_{\mathbf{I}}[k]\right)^{\top} \mathbf{M}^{\top}\mathbf{M} \left(\mathbf{I}[k] - \mathbf{y}_{\mathbf{I}}[k]\right), \tag{A40}$$

that is, $\mathbf{R}^{-1} = \mathbf{M}^{\top}\mathbf{M}$.

Appendix D. Numerical Considerations

In this section we describe numerical considerations that stabilize the recovery.

Appendix D.1. Hyper-Parameters

Our code requires the choice of hyper-parameters for rendering with vSHDOM [106] in `Step 1` and optimization with *scipy* L-BFGS [73,107] in `Step 2`. Table A2 summarizes the numerical parameters used in our simulations.

Table A2. Numerical parameters. For vSHDOM parameter definitions, see Ref. [106]. For L-BFGS parameter definitions, see Ref. [107].

vSHDOM			**L-BFGS**		
N_μ	N_ϕ	splitting accuracy	gtol	gtol	maxls
8	16	0.1	1×10^{-16}	1×10^{-16}	30

Appendix D.2. Preconditioning

Multivariate optimization can suffer from ill-conditioning due to different scales of the sought variables. This is expected when recovered variables represent different physical quantities with different units and orders of magnitude. A preconditioning of the update rule in (29) takes the following form

$$\Theta_{b+1} = \Theta_b - \chi_b \Pi^{-1} \nabla_{\Theta} \mathcal{D}\left(\mathbf{I}_{\Theta}, \mathbf{y}\right), \tag{A41}$$

where we apply a diagonal scaling matrix Π (*Jacobi* preconditioner) to scale the different physical variables $(\mathrm{LWC}, r_{\mathrm{e}})$. Thus, Π takes the form

$$\Pi = \mathrm{diag}\left(\Pi_{\mathrm{LWC}},\ \Pi_{r_{\mathrm{e}}}, ..., \Pi_{\mathrm{LWC}},\ \Pi_{r_{\mathrm{e}}}\right). \tag{A42}$$

In our tests, we use $\Pi_{\mathrm{LWC}} = 15$ and $\Pi_{r_{\mathrm{e}}} = 0.01$ to scale the parameters to a similar magnitude and closer to unity upon initialization.

Appendix D.3. Initialization

The recovery is initialized by the estimation of a cloud voxel mask, which bounds the cloud 3D shape. The 3D shape bound of the cloud is estimated using *Space-Carving* [37]. Space-carving is a

geometric approach to estimate a bound to 3D shape via multi-view images. The following steps are preformed in our space-carving algorithm

1. Each image is segmented into *potentially cloudy* and *non-cloudy* pixels (we use a simple radiance threshold).
2. From each camera viewpoint, each *potentially cloudy* pixel back-projects a ray into the 3D domain. Voxels that this ray crosses are voted as potentially cloudy.
3. Voxels which accumulate "cloudy" votes in at least 8 out of the 9 AirMSPI viewpoints are marked as cloudy.

Outside of the shape bound, LWC = 0 throughout iterations. Within the estimated cloud-shape bound, the volume content is initialized as homogeneous with LWC $= 0.01$ g/m^3, $r_e = 12\mu$m and $v_e = 0.1$. Then, inside of the shape-bound, {LWC,r_e,v_e} change throughout iterations, possibly diminishing LWC to very small values.

Appendix D.4. Convergence

Our approach alternates between `Step 1` (RTE rendering) and `Step 2` (approximate gradient) until convergence (Figure 7). The convergence criteria are dictated by the L-BFGS step: at each iteration, the relative change to the forward model and its gradient are compared to the *ftol* and *gtol* parameters (see Table A2 for values used). See *SciPy* documentation [107] for exact description of the L-BFGS stopping criteria.

References

1. Trenberth, K.E.; Fasullo, J.T.; Kiehl, J. Earth's global energy budget. *Bull. Am. Meteorol. Soc.* **2009**, *90*, 311–324. [CrossRef]
2. Boucher, O.; Randall, D.; Artaxo, P.; Bretherton, C.; Feingold, G.; Forster, P.; Kerminen, V.M.; Kondo, Y.; Liao, H.; Lohmann, U.; et al. Clouds and aerosols. In *Climate Change 2013: The Physical Science Basis. Contribution of Working Group I to the Fifth Assessment Report of the Intergovernmental Panel on Climate Change*; Cambridge University Press: Cambridge, UK, 2013; pp. 571–657.
3. Rosenfeld, D.; Lensky, I.M. Satellite-based insights into precipitation formation processes in continental and maritime convective clouds. *Bull. Am. Meteorol. Soc.* **1998**, *79*, 2457–2476. [CrossRef]
4. Platnick, S.; King, M.; Ackerman, S.; Menzel, W.; Baum, B.; Riedi, J.; Frey, R. The MODIS cloud products: Algorithms and examples from Terra. *IEEE Trans. Geosci. Remote Sens.* **2003**, *41*, 459–473. [CrossRef]
5. Marshak, A.; Platnick, S.; Várnai, T.; Wen, G.; Cahalan, R.F. Impact of three-dimensional radiative effects on satellite retrievals of cloud droplet sizes. *J. Geophys. Res. Atmos.* **2006**, *111*. [CrossRef]
6. Cho, H.M.; Zhang, Z.; Meyer, K.; Lebsock, M.; Platnick, S.; Ackerman, A.S.; Di Girolamo, L.; C.-Labonnote, L.; Cornet, C.; Riedi, J.; et al. Frequency and causes of failed MODIS cloud property retrievals for liquid phase clouds over global oceans. *J. Geophys. Res. Atmos.* **2015**, *120*, 4132–4154. [CrossRef]
7. National Academies of Sciences, Engineering, and Medicine. *Thriving on Our Changing Planet: A Decadal Strategy for Earth Observation from Space*; The National Academies Press: Washington, DC, USA, 2018.
8. Schilling, K.; Schechner, Y.Y.; Koren, I. CloudCT - computed tomography of clouds by a small satellite formation. In Proceedings of the IAA Symposium on Small Satellites for Earth Observation, Berlin, Germany, 6–10 May 2019.
9. Nakajima, T.; King, M.D. Determination of the optical thickness and effective particle radius of clouds from reflected solar radiation measurements. Part I: Theory. *J. Atmos. Sci.* **1990**, *47*, 1878–1893. [CrossRef]
10. Deschamps, P.Y.; Bréon, F.M.; Leroy, M.; Podaire, A.; Bricaud, A.; Buriez, J.C.; Seze, G. The POLDER mission: Instrument characteristics and scientific objectives. *IEEE Trans. Geosci. Remote. Sens.* **1994**, *32*, 598–615. [CrossRef]
11. Bréon, F.M.; Goloub, P. Cloud droplet effective radius from spaceborne polarization measurements. *Geophys. Res. Lett.* **1998**, *25*, 1879–1882. [CrossRef]

12. Kalashnikova, O.V.; Garay, M.J.; Davis, A.B.; Diner, D.J.; Martonchik, J.V. Sensitivity of multi-angle photo-polarimetry to vertical layering and mixing of absorbing aerosols: Quantifying measurement uncertainties. *J. Quant. Spectrosc. Radiat. Transf.* **2011**, *112*, 2149–2163. [CrossRef]
13. Lukashin, C.; Wielicki, B.A.; Young, D.F.; Thome, K.; Jin, Z.; Sun, W. Uncertainty estimates for imager reference inter-calibration with CLARREO reflected solar spectrometer. *IEEE Trans. Geosci. Remote. Sens.* **2013**, *51*, 1425–1436. [CrossRef]
14. Diner, D.; Xu, F.; Garay, M.; Martonchik, J.; Rheingans, B.; Geier, S.; Davis, A.; Hancock, B.; Jovanovic, V.; Bull, M.; et al. The Airborne Multiangle SpectroPolarimetric Imager (AirMSPI): A new tool for aerosol and cloud remote sensing. *Atmos. Meas. Tech.* **2013**, *6*, 2007–2025. [CrossRef]
15. Diner, D.J.; Boland, S.W.; Brauer, M.; Bruegge, C.; Burke, K.A.; Chipman, R.; Di Girolamo, L.; Garay, M.J.; Hasheminassab, S.; Hyer, E.; et al. Advances in multiangle satellite remote sensing of speciated airborne particulate matter and association with adverse health effects: From MISR to MAIA. *J. Appl. Remote. Sens.* **2018**, *12*, 042603. [CrossRef]
16. Martins, J.V.; Nielsen, T.; Fish, C.; Sparr, L.; Fernandez-Borda, R.; Schoeberl, M.; Remer, L. HARP CubeSat–An innovative hyperangular imaging polarimeter for earth science applications. In Proceedings of the Small Sat Pre-Conference Workshop, Logan, UT, USA, 3 August 2014; Volume 20.
17. Emde, C.; Barlakas, V.; Cornet, C.; Evans, F.; Korkin, S.; Ota, Y.; Labonnote, L.C.; Lyapustin, A.; Macke, A.; Mayer, B.; et al. IPRT polarized radiative transfer model intercomparison project—Phase A. *J. Quant. Spectrosc. Radiat. Transf.* **2015**, *164*, 8–36. [CrossRef]
18. Emde, C.; Barlakas, V.; Cornet, C.; Evans, F.; Wang, Z.; Labonotte, L.C.; Macke, A.; Mayer, B.; Wendisch, M. IPRT polarized radiative transfer model intercomparison project—Three-dimensional test cases (Phase B). *J. Quant. Spectrosc. Radiat. Transf.* **2018**, *209*, 19–44. [CrossRef]
19. Kak, A.; Slaney, M. *Principles of Computerized Tomographic Imaging IEEE Press*; IEEE Press: Piscataway, NJ, USA, 1988.
20. Gordon, R.; Bender, R.; Herman, G.T. Algebraic reconstruction techniques (ART) for three-dimensional electron microscopy and X-ray photography. *J. Theor. Biol.* **1970**, *29*, 471–481. [CrossRef]
21. Marshak, A.; Davis, A.; Cahalan, R.; Wiscombe, W. Nonlocal independent pixel approximation: Direct and inverse problems. *IEEE Trans. Geosci. Remote. Sens.* **1998**, *36*, 192–204. [CrossRef]
22. Faure, T.; Isaka, H.; Guillemet, B. Neural network retrieval of cloud parameters of inhomogeneous and fractional clouds: Feasibility study. *Remote Sens. Environ.* **2001**, *77*, 123–138. [CrossRef]
23. Faure, T.; Isaka, H.; Guillemet, B. Neural network retrieval of cloud parameters from high-resolution multispectral radiometric data: A feasibility study. *Remote Sens. Environ.* **2002**, *80*, 285–296. [CrossRef]
24. Cornet, C.; Isaka, H.; Guillemet, B.; Szczap, F. Neural network retrieval of cloud parameters of inhomogeneous clouds from multispectral and multiscale radiance data: Feasibility study. *J. Geophys. Res. Atmos.* **2004**, *109*, D12203. [CrossRef]
25. Zinner, T.; Mayer, B.; Schröder, M. Determination of three-dimensional cloud structures from high-resolution radiance data. *J. Geophys. Res. Atmos.* **2006**, *111*, D08204. [CrossRef]
26. Iwabuchi, H.; Hayasaka, T. A multi-spectral non-local method for retrieval of boundary layer cloud properties from optical remote sensing data. *Remote Sens. Environ.* **2003**, *88*, 294–308. [CrossRef]
27. Diner, D.J.; Beckert, J.C.; Reilly, T.H.; Bruegge, C.J.; Conel, J.E.; Kahn, R.A.; Martonchik, J.V.; Ackerman, T.P.; Davies, R.; Gerstl, S.A.W.; et al. Multi-angle Imaging SpectroRadiometer (MISR) instrument description and experiment overview. *IEEE Trans. Geosci. Remote Sens.* **1998**, *36*, 1072–1087. [CrossRef]
28. Marchand, R.; Ackerman, T. Evaluation of radiometric measurements from the NASA Multiangle Imaging SpectroRadiometer (MISR): Two-and three-dimensional radiative transfer modeling of an inhomogeneous stratocumulus cloud deck. *J. Geophys. Res. Atmos.* **2004**, *109*. [CrossRef]
29. Seiz, G.; Davies, R. Reconstruction of cloud geometry from multi-view satellite images. *Remote. Sens. Environ.* **2006**, *100*, 143–149. [CrossRef]
30. Cornet, C.; Davies, R. Use of MISR measurements to study the radiative transfer of an isolated convective cloud: Implications for cloud optical thickness retrieval. *J. Geophys. Res. Atmos.* **2008**, *113*. [CrossRef]
31. Evans, K.F.; Marshak, A.; Várnai, T. The Potential for Improved Boundary Layer Cloud Optical Depth Retrievals from the Multiple Directions of MISR. *J. Atmos. Sci.* **2008**, *65*, 3179–3196. [CrossRef]
32. Romps, D.M.; Öktem, R. Observing Clouds in 4D with Multiview Stereophotogrammetry. *Bull. Am. Meteorol. Soc.* **2018**, *99*, 2575–2586. [CrossRef]

33. Castro, E.; Ishida, T.; Takahashi, Y.; Kubota, H.; Perez, G.J.; Marciano, J.S. Determination of cloud-top Height through three-dimensional cloud Reconstruction using DIWATA-1 Data. *Sci. Rep.* **2020**, *10*, 1–13. [CrossRef]
34. Alexandrov, M.D.; Cairns, B.; Emde, C.; Ackerman, A.S.; Ottaviani, M.; Wasilewski, A.P. Derivation of cumulus cloud dimensions and shape from the airborne measurements by the Research Scanning Polarimeter. *Remote Sens. Environ.* **2016**, *177*, 144 – 152. [CrossRef]
35. Lee, B.; Di Girolamo, L.; Zhao, G.; Zhan, Y. Three-Dimensional Cloud Volume Reconstruction from the Multi-angle Imaging SpectroRadiometer. *Remote Sens.* **2018**, *10*, 1858. [CrossRef]
36. Yu, H.; Ma, J.; Ahmad, S.; Sun, E.; Li, C.; Li, Z.; Hong, J. Three-Dimensional Cloud Structure Reconstruction from the Directional Polarimetric Camera. *Remote Sens.* **2019**, *11*, 2894. [CrossRef]
37. Veikherman, D.; Aides, A.; Schechner, Y.Y.; Levis, A. Clouds in The Cloud. In Proceedings of the Asian Conference on Computer Vision (ACCV), Singapore, 1–5 November 2014; pp. 659–674.
38. Zinner, T.; Marshak, A.; Lang, S.; Martins, J.V.; Mayer, B. Remote sensing of cloud sides of deep convection: Towards a three-dimensional retrieval of cloud particle size profiles. *Atmos. Chem. Phys.* **2008**, *8*, 4741–4757. [CrossRef]
39. Alexandrov, M.D.; Miller, D.J.; Rajapakshe, C.; Fridlind, A.; van Diedenhoven, B.; Cairns, B.; Ackerman, A.S.; Zhang, Z. Vertical profiles of droplet size distributions derived from cloud-side observations by the research scanning polarimeter: Tests on simulated data. *Atmos. Res.* **2020**, *239*, 104924. [CrossRef] [PubMed]
40. Okamura, R.; Iwabuchi, H.; Schmidt, K.S. Feasibility study of multi-pixel retrieval of optical thickness and droplet effective radius of inhomogeneous clouds using deep learning. *Atmos. Meas. Tech.* **2017**, *10*, 4747–4759. [CrossRef]
41. Masuda, R.; Iwabuchi, H.; Schmidt, K.S.; Damiani, A.; Kudo, R. Retrieval of Cloud Optical Thickness from Sky-View Camera Images using a Deep Convolutional Neural Network based on Three-Dimensional Radiative Transfer. *Remote Sens.* **2019**, *11*, 1962. [CrossRef]
42. Liou, K.N.; Ou, S.C.; Takano, Y.; Roskovensky, J.; Mace, G.G.; Sassen, K.; Poellot, M. Remote sensing of three-dimensional inhomogeneous cirrus clouds using satellite and mm-wave cloud radar data. *Geophys. Res. Lett.* **2002**, *29*, 1360. [CrossRef]
43. Barker, H.; Jerg, M.; Wehr, T.; Kato, S.; Donovan, D.; Hogan, R. A 3D cloud-construction algorithm for the EarthCARE satellite mission. *Q. J. R. Meteorol. Soc.* **2011**, *137*, 1042–1058. [CrossRef]
44. Fielding, M.D.; Chiu, J.C.; Hogan, R.J.; Feingold, G. A novel ensemble method for retrieving properties of warm cloud in 3-D using ground-based scanning radar and zenith radiances. *J. Geophys. Res. Atmos.* **2014**, *119*, 10–912. [CrossRef]
45. Hasmonay, R.A.; Yost, M.G.; Wu, C.F. Computed tomography of air pollutants using radial scanning path-integrated optical remote sensing. *Atmos. Environ.* **1999**, *33*, 267–274. [CrossRef]
46. Todd, L.A.; Ramanathan, M.; Mottus, K.; Katz, R.; Dodson, A.; Mihlan, G. Measuring chemical emissions using an open-path Fourier transform infrared (OP-FTIR) spectroscopy and computer-assisted tomography. *Atmos. Environ.* **2001**, *35*, 1937–1947. [CrossRef]
47. Kazahaya, R.; Mori, T.; Kazahaya, K.; Hirabayashi, J. Computed tomography reconstruction of SO_2 concentration distribution in the volcanic plume of Miyakejima, Japan, by airborne traverse technique using three UV spectrometers. *Geophys. Res. Lett.* **2008**, *35*. [CrossRef]
48. Wright, T.E.; Burton, M.; Pyle, D.M.; Caltabiano, T. Scanning tomography of SO_2 distribution in a volcanic gas plume. *Geophys. Res. Lett.* **2008**, *35*. [CrossRef]
49. Warner, J.; Drake, J.; Snider, J. Liquid water distribution obtained from coplanar scanning radiometers. *J. Atmos. Ocean. Technol.* **1986**, *3*, 542–546. [CrossRef]
50. Huang, D.; Liu, Y.; Wiscombe, W. Determination of cloud liquid water distribution using 3D cloud tomography. *J. Geophys. Res. Atmos.* **2008**, *113*. [CrossRef]
51. Huang, D.; Liu, Y.; Wiscombe, W. Cloud tomography: Role of constraints and a new algorithm. *J. Geophys. Res. Atmos.* **2008**, *113*. [CrossRef]
52. Garay, M.J.; Davis, A.B.; Diner, D.J. Tomographic reconstruction of an aerosol plume using passive multiangle observations from the MISR satellite instrument. *Geophys. Res. Lett.* **2016**, *43*, 12–590. [CrossRef]
53. Aides, A.; Schechner, Y.Y.; Holodovsky, V.; Garay, M.J.; Davis, A.B. Multi-sky-view 3D aerosol distribution recovery. *Opt. Express* **2013**, *21*, 25820–25833. [CrossRef]

54. Geva, A.; Schechner, Y.Y.; Chernyak, Y.; Gupta, R. X-ray computed tomography through scatter. In Proceedings of the European Conference on Computer Vision (ECCV), Munich, Germany, 8–14 September 2018; pp. 34–50.
55. Arridge, S.R. Optical tomography in medical imaging. *Inverse Probl.* **1999**, *15*, R41. [CrossRef]
56. Boas, D.A.; Brooks, D.H.; Miller, E.L.; DiMarzio, C.A.; Kilmer, M.; Gaudette, R.J.; Zhang, Q. Imaging the body with diffuse optical tomography. *IEEE Signal Process. Mag.* **2001**, *18*, 57–75. [CrossRef]
57. Arridge, S.R.; Schotland, J.C. Optical tomography: Forward and inverse problems. *Inverse Probl.* **2009**, *25*, 123010. [CrossRef]
58. Che, C.; Luan, F.; Zhao, S.; Bala, K.; Gkioulekas, I. Inverse transport networks. *arXiv* **2018**, arXiv:1809.10820.
59. Evans, K.F. The spherical harmonics discrete ordinate method for three-dimensional atmospheric radiative transfer. *J. Atmos. Sci.* **1998**, *55*, 429–446. [CrossRef]
60. Doicu, A.; Efremenko, D.; Trautmann, T. A multi-dimensional vector spherical harmonics discrete ordinate method for atmospheric radiative transfer. *J. Quant. Spectrosc. Radiat. Transf.* **2013**, *118*, 121–131. [CrossRef]
61. Levis, A.; Schechner, Y.Y.; Aides, A.; Davis, A.B. Airborne three-dimensional cloud tomography. In Proceedings of the IEEE International Conference on Computer Vision (ICCV), Santiago, Chile, 7–13 December 2015; pp. 3379–3387.
62. Holodovsky, V.; Schechner, Y.Y.; Levin, A.; Levis, A.; Aides, A. In-situ multi-view multi-scattering stochastic tomography. In Proceedings of the IEEE International Conference on Computational Photography (ICCP), Evanston, IL, USA, 13–14 May 2016; pp. 1–12.
63. Levis, A.; Schechner, Y.Y.; Davis, A.B. Multiple-scattering microphysics tomography. In Proceedings of the IEEE Conference on Computer Vision and Pattern Recognition (CVPR), Honolulu, HI, USA, 21–26 July 2017; pp. 6740–6749.
64. Aides, A.; Levis, A.; Holodovsky, V.; Schechner, Y.Y.; Althausen, D.; Vainiger, A. Distributed Sky Imaging Radiometry and Tomography. In Proceedings of the IEEE International Conference on Computational Photography (ICCP), Saint Louis, MO, USA, 24–26 April 2020; pp. 1–12.
65. Loeub, T.; Levis, A.; Holodovsky, V.; Schechner, Y.Y.; Chernyak, Y.; Gupta, R. Monotonicity Prior for Cloud Tomography. In Proceedings of the European Conference on Computer Vision (ECCV), Glasgow, Scotlang, 24–29 August 2020.
66. Hansen, J.E. Multiple scattering of polarized light in planetary atmospheres, Part II. Sunlight reflected by terrestrial water clouds. *J. Atmos. Sci.* **1971**, *28*, 1400–1426. [CrossRef]
67. Marshak, A.; Davis, A. *3D Radiative Transfer in Cloudy Atmospheres*; Springer Science & Business Media: Berlin/Heidelberg, Germany, 2005.
68. Chylek, P. Extinction and liquid water content of fogs and clouds. *J. Atmos. Sci.* **1978**, *35*, 296–300.
69. Bohren, C.F.; Huffman, D.R. *Absorption and Scattering of Light by Small Particles*; John Wiley & Sons: Hoboken, NJ, USA, 2008.
70. Chandrasekhar, S. *Radiative Transfer*; Oxford University Press: Oxford, UK, 1950.
71. Mayer, B. Radiative transfer in the cloudy atmosphere. *Eur. Phys. J. Conf.* **2009**, *1*, 75–99. [CrossRef]
72. Nakajima, T.; Tanaka, M. Algorithms for radiative intensity calculations in moderately thick atmospheres using a truncation approximation. *J. Quant. Spectrosc. Radiat. Transf.* **1988**, *40*, 51–69. [CrossRef]
73. Zhu, C.; Byrd, R.H.; Lu, P.; Nocedal, J. Algorithm 778: L-BFGS-B: Fortran subroutines for large-scale bound-constrained optimization. *ACM Trans. Math. Softw.* **1997**, *23*, 550–560. [CrossRef]
74. Doicu, A.; Efremenko, D.S. Linearizations of the Spherical Harmonic Discrete Ordinate Method (SHDOM). *Atmosphere* **2019**, *10*, 292. [CrossRef]
75. Martin, W.; Cairns, B.; Bal, G. Adjoint methods for adjusting three-dimensional atmosphere and surface properties to fit multi-angle/multi-pixel polarimetric measurements. *J. Quant. Spectrosc. Radiat. Transf.* **2014**, *144*, 68–85. [CrossRef]
76. Martin, W.G.; Hasekamp, O.P. A demonstration of adjoint methods for multi-dimensional remote sensing of the atmosphere and surface. *J. Quant. Spectrosc. Radiat. Transf.* **2018**, *204*, 215–231. [CrossRef]
77. Forster, L.; Davis, A.B.; Diner, D.J.; Mayer, B. Toward Cloud Tomography from Space using MISR and MODIS: Locating the "Veiled Core" in Opaque Convective Clouds. *arXiv* **2019**, arXiv:1910.00077.
78. Zhao, M.; Austin, P.H. Life cycle of numerically simulated shallow cumulus clouds. Part II: Mixing dynamics. *J. Atmos. Sci.* **2005**, *62*, 1291–1310. [CrossRef]

79. Anderson, G.P.; Clough, S.A.; Kneizys, F.; Chetwynd, J.H.; Shettle, E.P. *AFGL Atmospheric Constituent Profiles (0.120 km)*; Technical Report; Air Force Geophysics Lab: Hanscom AFB, MA, USA, 1986.
80. Matheou, G.; Chung, D. Large-eddy simulation of stratified turbulence. Part 2: Application of the stretched-vortex model to the atmospheric boundary layer. *J. Atmos. Sci.* **2014**, *71*, 4439–4460. [CrossRef]
81. Yau, M.K.; Rogers, R.R. *A Short Course in Cloud Physics*; Elsevier: Amsterdam, The Netherlands, 1996.
82. Seethala, C. Evaluating the State-Of-The-Art of and Errors in 1D Satellite Cloud Liquid Water Path Retrievals with Large Eddy Simulations and Realistic Radiative Transfer Models. Ph.D. Thesis, University of Hamburg, Hamburg, Germany, 2012.
83. Ewald, F.; Zinner, T.; Kölling, T.; Mayer, B. Remote sensing of cloud droplet radius profiles using solar reflectance from cloud sides – Part 1: Retrieval development and characterization. *Atmos. Meas. Tech.* **2019**, *12*, 1183–1206. [CrossRef]
84. Alexandrov, M.D.; Cairns, B.; Emde, C.; Ackerman, A.S.; van Diedenhoven, B. Accuracy assessments of cloud droplet size retrievals from polarized reflectance measurements by the research scanning polarimeter. *Remote Sens. Environ.* **2012**, *125*, 92–111. [CrossRef]
85. Blyth, A.M.; Latham, J. A Climatological Parameterization for Cumulus Clouds. *J. Atmos. Sci.* **1991**, *48*, 2367–2371. [CrossRef]
86. French, J.R.; Vali, G.; Kelly, R.D. Observations of microphysics pertaining to the development of drizzle in warm, shallow cumulus clouds. *Q. J. R. Meteorol. Soc.* **2000**, *126*, 415–443. [CrossRef]
87. Gerber, H.E.; Frick, G.M.; Jensen, J.B.; Hudson, J.G. Entrainment, mixing, and microphysics in trade-wind cumulus. *J. Meteorol. Soc. Jpn. Ser. II* **2008**, *86*, 87–106. [CrossRef]
88. Khain, P.; Heiblum, R.; Blahak, U.; Levi, Y.; Muskatel, H.; Vadislavsky, E.; Altaratz, O.; Koren, I.; Dagan, G.; Shpund, J.; et al. Parameterization of Vertical Profiles of Governing Microphysical Parameters of Shallow Cumulus Cloud Ensembles Using LES with Bin Microphysics. *J. Atmos. Sci.* **2019**, *76*, 533–560. [CrossRef]
89. Pinsky, M.; Khain, A. Theoretical Analysis of the Entrainment–Mixing Process at Cloud Boundaries. Part I: Droplet Size Distributions and Humidity within the Interface Zone. *J. Atmos. Sci.* **2018**, *75*, 2049–2064. [CrossRef]
90. Bera, S.; Prabha, T.V.; Grabowski, W.W. Observations of monsoon convective cloud microphysics over India and role of entrainment-mixing. *J. Geophys. Res. Atmos.* **2016**, *121*, 9767–9788. [CrossRef]
91. Costa, A.A.; de Oliveira, C.J.; de Oliveira, J.C.P.; da Costa Sampaio, A.J. Microphysical observations of warm cumulus clouds in Ceara, Brazil. *Atmos. Res.* **2000**, *54*, 167–199. [CrossRef]
92. Lu, M.L.; Feingold, G.; Jonsson, H.H.; Chuang, P.Y.; Gates, H.; Flagan, R.C.; Seinfeld, J.H. Aerosol-cloud relationships in continental shallow cumulus. *J. Geophys. Res. Atmos.* **2008**, *113*. [CrossRef]
93. Martins, J.A.; Dias, M.A.F.S. The impact of smoke from forest fires on the spectral dispersion of cloud droplet size distributions in the Amazonian region. *Environ. Res. Lett.* **2009**, *4*, 015002. [CrossRef]
94. Hudson, J.G.; Noble, S.; Jha, V. Cloud droplet spectral width relationship to CCN spectra and vertical velocity. *J. Geophys. Res. Atmos.* **2012**, *117*. [CrossRef]
95. Pandithurai, G.; Dipu, S.; Prabha, T.V.; Maheskumar, R.S.; Kulkarni, J.R.; Goswami, B.N. Aerosol effect on droplet spectral dispersion in warm continental cumuli. *J. Geophys. Res. Atmos.* **2012**, *117*. [CrossRef]
96. Igel, A.L.; van den Heever, S.C. The Importance of the Shape of Cloud Droplet Size Distributions in Shallow Cumulus Clouds. Part I: Bin Microphysics Simulations. *J. Atmos. Sci.* **2017**, *74*, 249–258. [CrossRef]
97. Lu, M.L.; Seinfeld, J.H. Effect of aerosol number concentration on cloud droplet dispersion: A large-eddy simulation study and implications for aerosol indirect forcing. *J. Geophys. Res. Atmos.* **2006**, *111*, D02207. [CrossRef]
98. Wang, X.; Xue, H.; Fang, W.; Zheng, G. A study of shallow cumulus cloud droplet dispersion by large eddy simulations. *Acta Meteorol. Sin.* **2011**, *25*, 166–175. [CrossRef]
99. Milbrandt, J.A.; Yau, M.K. A Multimoment Bulk Microphysics Parameterization. Part I: Analysis of the Role of the Spectral Shape Parameter. *J. Atmos. Sci.* **2005**, *62*, 3051–3064. [CrossRef]
100. Cairns, B.; Russell, E.E.; Travis, L.D. Research Scanning Polarimeter: Calibration and ground-based measurements,. In *Polarization: Measurement, Analysis, and Remote Sensing II*; International Society for Optics and Photonics, Bellingham, WA, USA, 1999; Volume 3754, pp. 186–196.
101. Levis, A.; Loveridge, J.; Aides, A. Pyshdom. 2020. Available online: https://github.com/aviadlevis/pyshdom (accessed on 1 January 2020).

102. Sanghavi, S.; Davis, A.B.; Eldering, A. vSmartMOM: A vector matrix operator method-based radiative transfer model linearized with respect to aerosol properties. *J. Quant. Spectrosc. Radiat. Transf.* **2014**, *133*, 412–433. [CrossRef]
103. Xu, F.; Davis, A.B. Derivatives of light scattering properties of a nonspherical particle computed with the T-matrix method. *Opt. Lett.* **2011**, *36*, 4464–4466. [CrossRef]
104. Florescu, L.; Markel, V.A.; Schotland, J.C. Inversion formulas for the broken-ray Radon transform. *Inverse Probl.* **2011**, *27*, 025002. [CrossRef]
105. Van Harten, G.; Diner, D.J.; Daugherty, B.J.; Rheingans, B.E.; Bull, M.A.; Seidel, F.C.; Chipman, R.A.; Cairns, B.; Wasilewski, A.P.; Knobelspiesse, K.D. Calibration and validation of Airborne Multiangle SpectroPolarimetric Imager (AirMSPI) polarization measurements. *Appl. Opt.* **2018**, *57*, 4499–4513. [CrossRef]
106. Pincus, R.; Evans, K.F. Computational cost and accuracy in calculating three-dimensional radiative transfer: Results for new implementations of Monte Carlo and SHDOM. *J. Atmos. Sci.* **2009**, *66*, 3131–3146. [CrossRef]
107. Scipy. L-BFGS-B. 2020. Available online: https://docs.scipy.org/doc/scipy/reference/optimize.minimize-lbfgsb.html (accessed on 1 January 2020).